

Seasonal variation of Saturn’s Lyman- α brightness

P. STEPHENSON,¹ T. T. KOSKINEN,¹ Z. BROWN,¹ E. QUÉMERAIS,² P. LAVVAS,³ J. I. MOSES,⁴ B. SANDEL,¹ AND R. YELLE¹

¹*Lunar and Planetary Laboratory, University of Arizona, Tucson, AZ, USA*

²*LATMOS/IPSL, Université de Versailles Saint-Quentin, Guyancourt, France*

³*GSMA, Université de Reims, Reims, France*

⁴*Space Science Institute, Boulder, CO, USA*

ABSTRACT

We examine Saturn’s non-auroral (dayglow) emissions at Lyman- α observed by the Cassini/UVIS instrument from 2004 until 2016, to constrain meridional and seasonal trends in the upper atmosphere. We separate viewing geometry effects from trends driven by atmospheric properties, by applying a multi-variate regression to the observed emissions. The Lyman- α dayglow brightnesses depend on the incident solar flux, solar incidence angle, emission angle, and observed latitude. The emissions across latitudes and seasons show a strong dependence with solar incidence angle, typical of resonantly scattered solar flux and consistent with no significant internal source. We observe a bulge in Ly- α brightness that shifts with the summer season from the southern to the northern hemisphere. We estimate atomic hydrogen optical depths above the methane homopause level for dayside disk observations (2004-2016) by comparing observed Lyman- α emissions to a radiative transfer model. We model emissions from resonantly scattered solar flux and a smaller but significant contribution by scattered photons from the interplanetary hydrogen (IPH) background. During northern summer, inferred hydrogen optical depths steeply decrease with latitude towards the winter hemisphere from a northern hemisphere bulge, as predicted by a 2D seasonal photochemical model. The southern hemisphere mirrors this trend during its summer. However, inferred optical depths show substantially more temporal variation between 2004 and 2016 than predicted by the photochemical model.

Keywords: Planetary atmospheres (1244) — Saturn (1426) — Ultraviolet astronomy (1736) — Upper atmosphere (1748) — Atmospheric variability (2119)

1. INTRODUCTION

Lyman- α is the brightest ultraviolet emission line in the solar system and has been observed at Saturn since 1976, initially with sounding rockets and the Copernicus satellite (Weiser et al. 1977; Barker et al. 1980). Subsequent observations of Lyman- α emissions from Saturn were made by the Interplanetary Ultraviolet Explorer (IUE, Clarke et al. 1981; McGrath & Clarke 1992) and during the Voyager flybys with the Ultraviolet Spectrometer (UVS, Broadfoot et al. 1981; Sandel et al. 1982; Ben-Jaffel et al. 1995). Over its 13-year mission, Cassini/Huygens (Matson et al. 2002) orbited Saturn, compiling an extensive dataset of Lyman- α emissions with the Ultraviolet Imaging Spectrograph (UVIS, Esposito et al. 2005).

Recently, Ben-Jaffel et al. (2023) identified a bulge in Lyman- α emissions from Saturn’s thermosphere in the northern hemisphere between latitudes of 5 and 35° N, with observations from the Hubble Space Telescope’s

Space Telescope Imaging Spectrograph (HST/STIS) and Cassini/UVIS. They also identified the same bulge in Voyager/UVS observations that probed Saturn’s atmosphere close to the northern spring equinox 35 years earlier (Yelle et al. 1986). They concluded that the observed northern hemisphere bulge is a permanent feature of the thermosphere. We note that this bulge shows no longitudinal variation and therefore differs significantly from the Lyman- α bulge that has been observed on Jupiter, which is fixed in system III longitude (Sandel et al. 1980; Clarke et al. 1980; Dessler et al. 1981; Skinner et al. 1988). Ben-Jaffel et al. (2023) proposed two primary mechanisms to drive the emission bulge: variation of the temperature profile in the lower thermosphere and upper stratosphere or a previously unidentified suprathermal atomic hydrogen population at high altitudes, both of which could vary seasonally. They proposed that the suprathermal population could be created, for example, by a significant influx of material from

the rings or Enceladus into the upper atmosphere. In this study, we examine Lyman- α emissions over the duration of the Cassini mission, in order to examine the cause of the bulge, whether it is a permanent feature of Saturn’s thermosphere, and the source of the increased emissions.

At Lyman- α , Cassini/UVIS consistently observed much lower disk brightnesses compared to the observations of Voyager/UVS, with peak brightnesses of about 1 kR outside the auroral oval compared to 3-4 kR during the Voyager flybys (Ben-Jaffel et al. 1995; Gustin et al. 2010; Shemansky et al. 2009; Koskinen et al. 2020). Gustin et al. (2010) suggested that the disparity was a result of ring-reflected light during the Voyager observations, while Shemansky et al. (2009) suggested strong electroglow emissions could reconcile the differences. The Voyager brightnesses have since been questioned and revised downward by Quémerais et al. (2013a), who concluded that the sensitivity of the Voyager/UVS instruments were underestimated by a factor of 1.5-2.5. The revised Voyager Lyman- α brightnesses are roughly consistent with those observed by Cassini/UVIS (Koskinen et al. 2020). Using HST observations from Earth orbit as a calibration standard, Ben-Jaffel et al. (2023) challenged the downward revision of the Voyager brightnesses and proposed instead a recalibration of the Cassini/UVIS instrument at Lyman- α that would increase the observed brightnesses by 70%. After scaling with the solar Lyman- α flux at different times, they compared several observations by Cassini/UVIS (in 2007, 2013 and 2014), HST/STIS (in 2017) and HST’s Goddard High Resolution Spectrograph (in 1996) to arrive at this conclusion.

Cross-calibration of UV instruments between missions at Lyman- α remains difficult. Observations of Lyman- α emissions from interplanetary background hydrogen provide one method to facilitate it. Observations of the IPH Lyman- α by the Voyager/UVS instruments (Katushkina et al. 2016, 2017), New Horizons Alice (Gladstone et al. 2018, 2021) and future observations by PHEBUS on Bepi/Colombo (Quémerais et al. 2020), have and will continue to constrain models of the IPH background (e.g. Quémerais & Izmodenov 2002; Quémerais et al. 2013b; Izmodenov et al. 2013; Pryor et al. 2022). Models of the interaction between the local interstellar medium and the solar wind (Quémerais et al. 2006; Izmodenov et al. 2001, 2013) are dependent on the hydrogen density of the local interstellar medium (LISM) and at the terminator shock near 90 au, with estimates of the LISM Hydrogen density varying from 0.12 to 0.195 cm^{-3} (Dialynas et al. 2019; Swaczyna et al. 2020). In addition to scattered solar flux, a galactic contribution to

the background of 40 R has been identified at large heliocentric distances (Gladstone et al. 2021; Pryor et al. 2022). While there remains uncertainty on the density of the LISM, we compare Cassini/UVIS Lyman α observations to the model of (Quémerais et al. 2013a) and find good agreement between Cassini/UVIS observed and modelled brightnesses, without the proposed recalibration by a factor 1.7 (Ben-Jaffel et al. 2023; Pryor et al. 2024). The situation with regard to calibration, however, is clearly confusing and based on this, we cannot entirely discount the possibility of a significant uncertainty in Saturn’s Lyman- α brightness.

Limb observations and solar occultations, in conjunction with photochemical models, can provide further constraints on the atomic hydrogen columns and Lyman- α emissions.

In addition to the Lyman- α bulge, Saturn’s thermosphere also exhibits latitudinal variation in temperature (Brown et al. 2020) and exobase altitude that are likely to be seasonally variable (Koskinen et al. 2021). Stellar occultations by Cassini/UVIS have constrained the temperature of Saturn’s thermosphere, allowing the retrieval of density profiles of upper atmospheric constituents, including H_2 , He and CH_4 (Koskinen et al. 2013, 2015, 2016; Koskinen & Guerlet 2018; Shemansky & Liu 2012; Brown et al. 2020, 2022). Stellar occultations, when stable, are essentially self-calibrating and independent of instrument calibration. We note, however, that stellar occultations cannot be used to retrieve the density of H.

Latitudinal and seasonal trends in the upper atmosphere have been predicted by photochemical models (Moses et al. 2000a; Moses & Bass 2000; Moses & Greathouse 2005; Hue et al. 2015, 2016). This is because, for example, hydrocarbons in the stratosphere are influenced by meridionally-varying insolation, including changes due to the motion of the ring shadow across Saturn’s disk (Moses & Greathouse 2005). The variation of methane in the stratosphere also has substantial impact on atomic hydrogen through both the production of H through photolysis (Moses et al. 2000a) and the location of the homopause. Comparison of photochemical models with Lyman- α observations from Cassini/UVIS can constrain the hydrogen column above the methane homopause, with methane a strong absorber at Lyman- α . This can subsequently constrain eddy mixing and circulation near the homopause level (Atreya 1982; Sandel et al. 1982; Atreya et al. 1984; Emerich et al. 1993; Moses et al. 2000a; Moses & Greathouse 2005).

The emissions of Lyman- α from Saturn’s disk, observed by Cassini/UVIS, provide an extensive dataset over 13 years, with coverage across all latitudes. Koskinen et al. (2020) examined one observational sequence of

Lyman- α from the Saturn disk in 2007. They found the brightnesses were consistent with resonance scattering of solar flux by a hydrogen column of $3 \times 10^{16} \text{ cm}^{-3}$, in agreement with columns calculated with a photochemical model (Moses & Bass 2000; Moses et al. 2000b; Moses & Greathouse 2005). Several other case studies have been examined (Mitchell et al. 2009; Shemansky et al. 2009; Gustin et al. 2010; Koskinen et al. 2020; Ben-Jaffel et al. 2023), but the full Lyman- α emission dataset has not yet been fully explored.

By comparing results from a radiative transfer model with Cassini UVIS observations, we can estimate the effective optical depth of the atomic hydrogen layer. We follow the approach of Yelle et al. (1989) who modelled resonance scattering of a deep atmosphere by the iterative doubling and adding of thin layers, using angle-averaged partial frequency redistribution. We examine the variation of the effective hydrogen optical depths with latitude and season, under the assumption that emissions are dominated by resonant scattering by the ambient, thermal hydrogen population. In addition, we directly compare the inferred effective optical depths to the results of a seasonal photochemical model, to identify processes not included in the photochemical model, and to identify discrepancies that might indicate the presence of suprathermal atoms or internal emissions generated by photoelectron or energetic particle impact.

In this study, we examine the extensive dataset of Lyman- α emissions from Saturn’s dayside disk collected by Cassini UVIS from 2004 to the end of 2016. We consider the Lyman- α observations through three approaches, with the methods used outlined in Section 2. In section 3.1, we compare observation of the IPH Lyman- α background to the model of Quémerais et al. (2013b). In Section 3.2, we employ a multi-variate analysis of the Lyman- α observations to confirm that resonance scattering of solar flux is a dominant source of the emissions from Saturn’s non-auroral, dayside disk. Finally, in Section 3.3, we compare the radiative transfer model, based on doubling and adding of thin layers, to the Lyman- α observations, and we retrieve the H optical depth above the methane homopause across the mission, to determine seasonal variation of Saturn’s thermosphere. We discuss the results in Section 4, in particular with relation to the nature of the Lyman- α bulge. We also compare a seasonal photochemical model to the effective H optical depths retrieved in Section 3.3.

2. METHODS

2.1. Cassini UVIS data

We consider Cassini/UVIS observations from 2003 until 2016 during Cassini’s orbits of Saturn, including MO-

SAIC, EUVFUV and COMPSIT/CIRS scans identified in the Planetary Data System. This first survey of the emission data focuses on nadir observations. Limb scans will not be considered in this work and are instead the subject of a future paper. The Cassini/UVIS instrument comprised 64 spatial bins along the slit and 1024 spectral bins with a resolution of 0.78 \AA . We focus on Lyman- α emissions from Saturn’s disk using the FUV channel of UVIS (1115 to 1912 \AA), integrating the emission brightness between 1205 and 1225 \AA . We use the time-dependent sensitivity and flat field updates that indicate a degradation of the signal by 30% from launch to the end of the mission but in our default models, we do not use the proposed recalibration of the Cassini/UVIS instrument by a factor 1.7 at Lyman- α (Ben-Jaffel et al. 2023, p24). While additional degradation at Lyman-alpha would not be surprising, cross-calibrating instruments with different viewing geometries and the use of IPH models for calibration also includes uncertainties. For example, our IPH model produces Lyman- α brightnesses consistent with UVIS observations without the additional calibration factor (see Section 3.1). The effective optical depths predicted by photochemical models of Saturn’s atmosphere are also more consistent with UVIS observations with the previous calibration (see Section 3.3). In addition, we note that a calibration uncertainty of a factor 2 does not affect our results with respect to both seasonal and meridional trends observed in the Lyman- α emission.

In order to reduce the downlink data volume and increase spatial coverage, the wavelength range of observations was sometimes reduced and neighbouring spectral pixels were combined (typically with a bin width of 4 pixels). In cases with no spectral binning, we use the Cube Generator from the Cassini/UVIS team and the pipeline flatfield to process the data. When spectral binning was applied, the pipeline flatfield does not appropriately address the presence of ‘evil’ pixels on the detector, which returned much lower signals than those surrounding them. In the pipeline calibration the intensity is interpolated to the ‘evil’ pixels, which are assigned the value NaN in the flatfield. With binned spectra, one evil pixel in the bin results in a NaN value for the whole bin, losing information from the adjacent pixels. In these cases, we process the data with the Cube Generator with no flatfield, applying the derived 2007 flatfield correction of (Koskinen et al. 2020) for binned data. The only observations that use spectral binning occur between 2004 and 2008, and we do not expect a substantial change in the flatfield correction over this period.

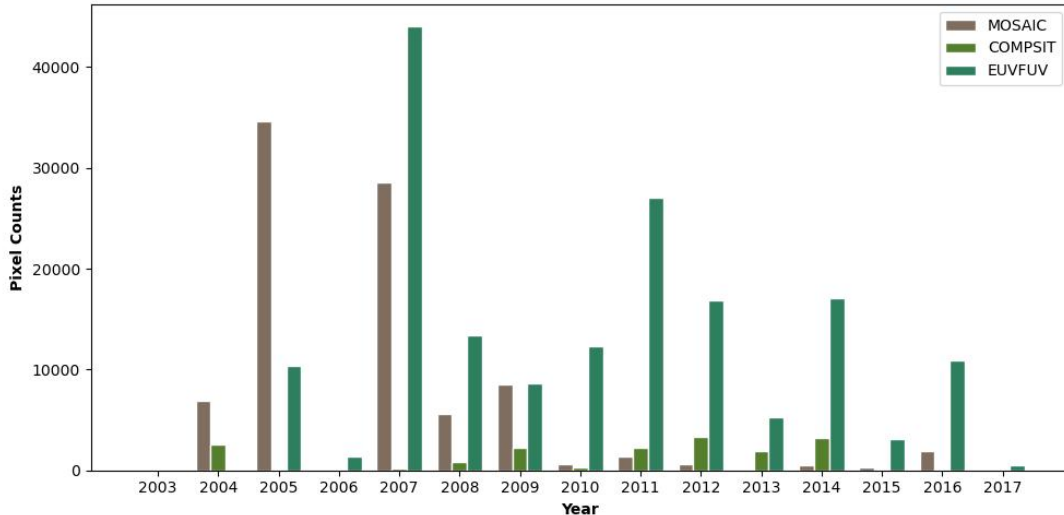


Figure 1. Number of observation pixels on Saturn’s dayside disk, outside the auroral regions ($|\phi_{lat}| < 65^\circ$) by year and observation type (see text for an explanation of the types).

The three observation classes (MOSAIC, EUVFUV and COMPSIT/CIRS) had different aims and characteristics. MOSAIC observations were designed to maximise spatial coverage, observing much or all of the Saturn system (including the rings). Prior to 2008, spectral binning of width 4 was common allowing integration times of 25 to 95s. After 2008, the MOSAIC observations did not use any spectral binning and required longer integration times from 120 to 900s. During EUVFUV observations, spectra from both the EUV and FUV channels were retrieved, with no spectral binning. These often capture a substantial part of the Saturn system, such as in Figure 2, using an integration time between 180 and 260s. Finally, the COMPSIT/CIRS observations were paired with observations by the Cassini/Composite Infrared Spectrometer (CIRS, Flasar et al. 2005). These do not use any spectral binning and have much smaller spatial coverage, often only observing along a single line across Saturn’s disk and limb. However, the long integration times (1200 or 2400s) provide excellent signal-to-noise ratios for the spectra.

The UVIS dataset comprises 636 observations over 14 years comprising 140,925 scans and 8,032,725 pixels, of which 3,000,000 are on the dayside of Saturn’s disk. In this study, we focus on airglow emissions and therefore exclude the auroral regions with latitudes poleward of 60° . Figure 1 shows the number of observation pixels by observation type and year. Additionally, over large periods much of Saturn’s disc was shadowed by the Saturnian rings. We do not have a good constraint on the solar flux entering the atmosphere after absorption in the ring atmosphere, so these points are removed from the dataset. For each observation, the ring shadow re-

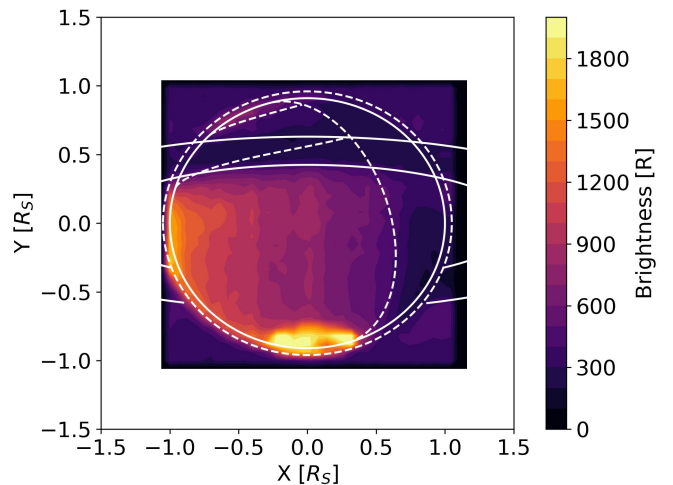


Figure 2. Observed Lyman- α emission brightness from Saturn on 21 Jun 2005. The solid white lines outline Saturn’s disk and its rings. Dashed lines show the ring shadow region (at this time in the northern hemisphere), the terminator, and the position of the exobase.

gion and rings are mapped onto the surface of Saturn (e.g. see Figure 2).

2.2. Multivariate quadratic regression of UVIS data

In this section, we outline a data based approach to the analysis of the Lyman- α emissions from Saturn, which is independent of radiative transfer modelling. This helps to identify the key emission source of Lyman- α at Saturn and to test the assumptions used in the RT model. For this purpose, we consider emission observations from 2014 until the end of mission, from MOSAIC, EUVFUV, and COMPSIT/CIRS observations. We primarily focus

on part of the northern hemisphere summer (2014-2016), such that the meridional trends in the atmosphere and emissions do not change substantially with time.

We use a multi-variate regression with independent variables of emission angle, incidence angle and latitude, which are used to predict the observed Lyman- α brightness. For simplicity, we have removed the dependence on the solar flux variation by scaling all the brightnesses to the solar flux applicable on 1 Jan 2016 (see Section 2.3.1). We choose these variables because resonance scattering is strongly dependent on the solar incidence angle and the emission angle of the observation, and because previous studies have identified meridional trends in the Lyman- α emissions. The model includes a quadratic in emission and incidence angles, in addition to a cubic in latitude. The full expression used for the regression is:

$$B = p_0 + p_1 \cdot \theta_{em} + p_2 \cdot \theta_{in} + p_3 \cdot \phi_{lat} + p_4 \cdot \theta_{em}^2 + p_5 \cdot \theta_{em} \cdot \theta_{in} + p_6 \cdot \theta_{in}^2 + p_7 \cdot \phi_{lat}^2 + p_8 \cdot \phi_{lat}^3, \quad (1)$$

with p_i the coefficients, θ_{em} is the emission angle, θ_{in} is the solar incidence angle, and ϕ_{lat} is the planetocentric latitude. We prepare the data by standardizing the independent variables ($\theta_{em}, \theta_{in}, \phi_{lat}$), and then transforming them into the required polynomial expressions in Eq. 1. The 86,913 pixels in the NH summer were randomly split by 80% to 20% into training and testing sets, respectively. The model was then trained using a least-squares regression. Monte-Carlo analysis was used to retrieve confidence intervals for the coefficients, resampling the dataset 1000 times.

2.3. Radiative transfer modeling

In order to constrain the properties of the atmosphere, we model the brightness of scattered solar and IPH Lyman- α using a radiative transfer model based on doubling and adding, which includes an angular dependent frequency redistribution function (Yelle 1988; Yelle & Wallace 1989; Wallace et al. 1989). The model is based on assumptions of a plane-parallel and isothermal atmosphere. The plane-parallel assumption breaks down for observations close to either the limb or the terminator, as the incidence or emission angles near 90° . Consequently, we only apply the model to cases of $\theta_{em} < 60^\circ$ and $\theta_{in} < 65^\circ$. Thin layer approximations of scattering and transmission functions (outlined in Appendix B Yelle 1988) are iteratively doubled in thickness (see Appendix A), computing new scattering, transmission and extinction functions until the required optical depth is reached.

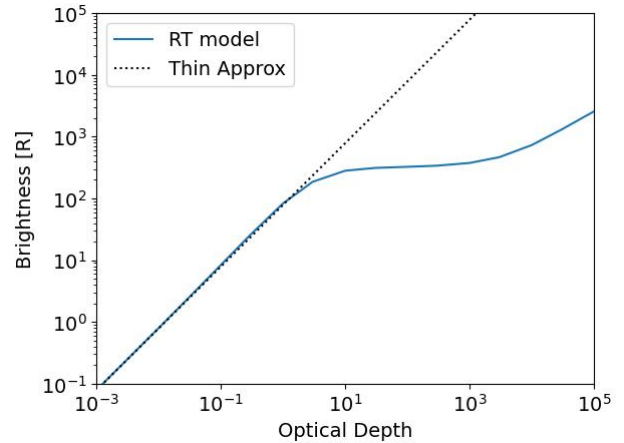


Figure 3. (blue) Brightness vs. optical depth for resonance scattering of Lyman- α by atomic hydrogen for $(\theta_{in}, \theta_{em}) = (0, 0)$. The optically thin approximation is given by the black dotted line.

The scattering and transmission functions are dependent on the atmospheric temperature (via the Lyman- α lineshape in the thermosphere) and the optical depth. We use a thermospheric temperature that varies with latitude, based on the pole-to-pole map of stellar occultations of Cassini/UVIS throughout 2017 (see Section 2.3.3; Brown et al. 2020). Figure 3 shows the variation in brightness as the atomic H optical depth increases, for the nadir case $(\theta_{in}, \theta_{em}) = (0, 0)$. The approximation for an optically thin atmosphere is given by the dotted line. The RT model is identical to the optically thin approximation at small optical depths, before deviating as it approaches $\tau = 1$. Beyond this, the atmosphere is optically thick and the output brightness varies little as the column grows. At $\tau = 10^3$, the brightness then begins to increase once again, as frequency redistribution becomes more effective and photons in the Lorentzian wings begin to be multiply scattered. For deep atmospheres, like Saturn's, the frequency redistribution is critical to computing the scattered brightness, due to the scattering of photons initially far from the line centre.

2.3.1. Scattered solar flux

For scattered solar flux, the brightness of Lyman- α is dependent on the magnitude and shape of the solar flux entering the top of the atmosphere. The RT code is normalised to the solar flux at line center. For the magnitude of the flux, we use the LISIRD composite Lyman- α database (Machol et al. 2019), which is based on fluxes measured at 1 AU by various instruments (e.g. Hinteregger et al. 1981; Barth et al. 1983; Woods et al. 2000; McClintock et al. 2005). First, we correct the LISIRD date for the flux to match the solar longitude at Saturn during the UVIS observation, which requires a shift

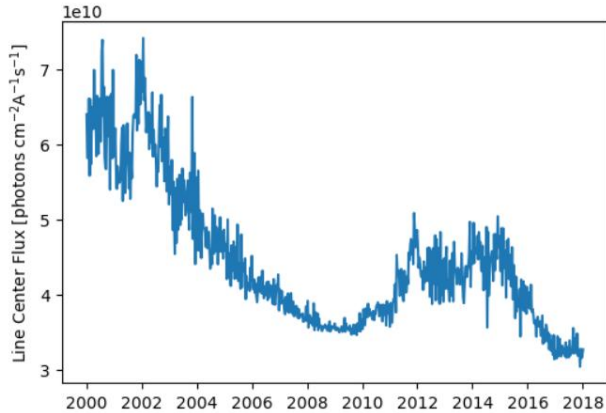


Figure 4. Lyman- α flux at Saturn throughout the Cassini mission, extrapolated from LISIRD fluxes at 1 AU. This does not include absorption of the solar flux between 1 AU and Saturn, which is accounted for separately.

of up to 15 days depending on the relative positions of Earth and Saturn. This is converted to a line center flux using the line shape from [Lemaire et al. \(2005\)](#), imposed at 1 AU (see Figure 5). After this, we extrapolate the flux to Saturn using an inverse square law with heliocentric distance (see Figure 4). We include absorption of the solar flux between 1 AU and Saturn by the IPH background, using the IPH model described in Section 2.3.2. Once normalised, the modelled brightness based on scattered solar flux from Saturn’s atmosphere is interpolated to the emission and solar incidence angle of a given observation, giving brightness as a function of temperature, effective H column optical depth, and viewing geometry. The temperature is constrained by a fit with latitude to the results retrieved from stellar occultations of the thermosphere (see Section 2.3.3).

2.3.2. Lyman- α from the interplanetary background

Lyman- α flux emitted by the IPH background is also scattered by Saturn’s upper atmosphere. Unlike the solar flux, the IPH Lyman- α radiation covers the sky, so we integrate the IPH flux that enters from all directions (see Appendix C for further details). The flux entering the atmosphere from each direction is calculated with an IPH background model of [Quémerais et al. \(2013a\)](#). This model incorporates angular dependent partial frequency redistribution to treat resonant scattering of solar Lyman- α radiation by the interplanetary hydrogen distribution ([Quémerais 2000](#); [Quémerais et al. 2003](#)). The distribution is calculated from the interaction of the local interstellar medium with the solar wind ([Izmodenov et al. 2001, 2013](#)), using a hydrogen density of $n_{H,TS} = 0.09 \text{ cm}^{-3}$ and $n_H = 0.14 \text{ cm}^{-3}$ in the local interstellar medium ([Bzowski et al. 2009](#); [Izmodenov & Alexashov 2020](#)). We do not include an additional

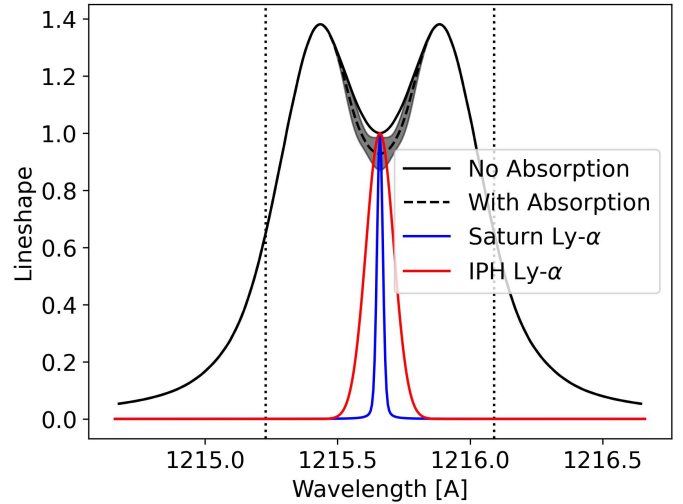


Figure 5. (black solid line) Lineshape of the solar Lyman α flux (black) at 1au normalised to 1 at the linecentre. (black dashed line and shaded region) Lineshape of solar Lyman- α after absorption of solar flux by the IPH background. (blue) The Voigt profile of Lyman- α in Saturn’s thermosphere for a temperature of 350K. (red) The lineshape of the IPH Lyman- α entering the upper atmosphere at $T_{IPH} = 10,000$ K. The dotted vertical lines show the integration limits of $\pm 44\Delta\nu_{D,Sat}$, used in the radiative transfer model.

contribution of a 40 R galactic contribution ([Gladstone et al. 2021](#); [Pryor et al. 2022](#)) that is isotropic. However, at distances of 9-10 au the galactic contribution is small in comparison to IPH-scattered solar flux. The brightness, line width and temperature of the IPH Lyman- α is calculated by integrating the emissions along the line-of-sight.

The brightness of the IPH emission line varies strongly with direction of observation, being largest close to the sunward direction when at large heliocentric distances. The position of the observer relative to the flow of the local interstellar medium also impacts the variation of Lyman- α with line-of-sight, although to a lesser extent. Here, we consider two positions in the IPH: the position of Saturn in 2006 and 2016. In both cases, we construct a full sky map of the Lyman- α brightness at the position of Saturn (e.g. Figure 6a). The IPH Lyman- α brightness can be parameterised as a function of the angle to the direction of maximum brightness (θ_{Max} , Fig. 6b). We fit this as a sum of a quadratic and an exponential with respect to $\cos\theta_{max}$. At heliocentric distances of 10 AU, the maximum in the IPH density and Lyman- α brightness are closely aligned with the sunward direction.

2.3.3. Hydrogen effective optical depths

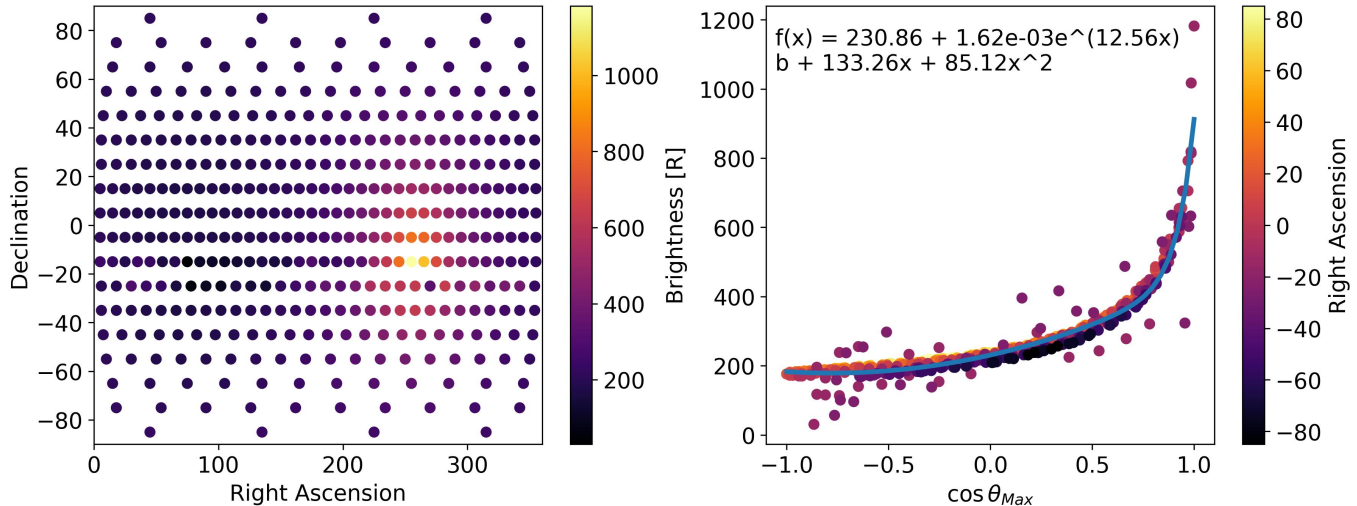


Figure 6. (left) Full sky map of IPH brightness at Saturn in 2016, modelled as described in Section 2.3.2. (right) Modelled IPH Lyman- α brightness against angle to direction of maximum brightness. The fit to the IPH brightness is shown in blue.

The radiative transfer model, combining scattering of solar and IPH Lyman- α photons is used to calculate brightness as a function of the optical depth of the effective H column in the atmosphere, emission and incidence angle, and atmospheric temperature $B_{RT}(\tau_H, \theta_{em}, \theta_{in}, T_{Sat})$. By effective optical depth, we refer to the vertical Lyman- α line center optical depth of the H column above the methane homopause. It is important to note that we assume all light at Lyman- α to be absorbed below the homopause. We do not self-consistently simulate absorption by CH_4 because seasonal changes to the depth of the homopause are not known a priori. This effort represents the first, zeroth order effort to constrain variations in the effective H scattering column in the thermosphere. We have therefore chosen to follow this simplified, retrieval-type approach in our modeling.

We use a variable temperature profile with latitude, based on stellar occultations by UVIS (Brown et al. 2020) combined with CIRS limb scans (Brown et al. 2024; Guerlet et al. 2018; Koskinen & Guerlet 2018). Thermal structure is also expected to be seasonally variable but the general characteristics of the temperature distribution, including the gradient between the auroral regions and the equator, are relatively stable, even on multi-decadal timescales (Koskinen et al. 2021). We calculate the pressure averaged temperatures ($\bar{T}_P = 1/[\ln(p_1/p_0)] \int_{P_0}^{P_1} T(d \ln P)$) above the methane homopause, which are then fit with a 6th-order polynomial (red, Figure 8). Here, the CH_4 homopause is defined as the location where $\tau_{\text{CH}_4} = 1$ at Lyman- α in the atmospheric structure models fitted to the occultations and CIRS observations (e.g., Brown et al. 2024; Koskinen & Guerlet 2018). As noted above, the homopause

location is obviously expected to change over time but the pressure-averaged temperatures are nevertheless assumed to remain relatively stable. The polynomial fit is used to convert the latitude of observation into an atmospheric temperature in the radiative transfer model.

For each pixel, characterised by incidence angle, emission angle and latitude (temperature), the brightness against optical depth is interpolated to the viewing geometry. Using this monotonic relationship, the observed Lyman- α brightness for each pixel is converted to an effective hydrogen optical depth for each pixel (Figure 7). We use Monte Carlo error estimation, allowing for uncertainty in the Lyman- α brightness from the UVIS instrument, as well as uncertainty in the solar flux normalisation and absorption of the solar flux between the Sun and Saturn.

2.3.4. Other sources of Lyman- α

In comparing the radiative transfer model with the observed brightnesses, we ignore the possibility of internal sources and scattering by suprathermal atomic H. However, we considered the following potential emission sources that are likely to be insignificant:

- photoelectron impact excitation
- H^+ recombination
- scattering by hot hydrogen in the thermosphere, produced via H_3^+ recombination.

Waite et al. (1983) used a two-stream model to examine Lyman- α emissions driven by photoelectrons at Jupiter, finding a total contribution of 26 R. Extrapolating this to Saturn, we expect a factor 3-4 reduction in the

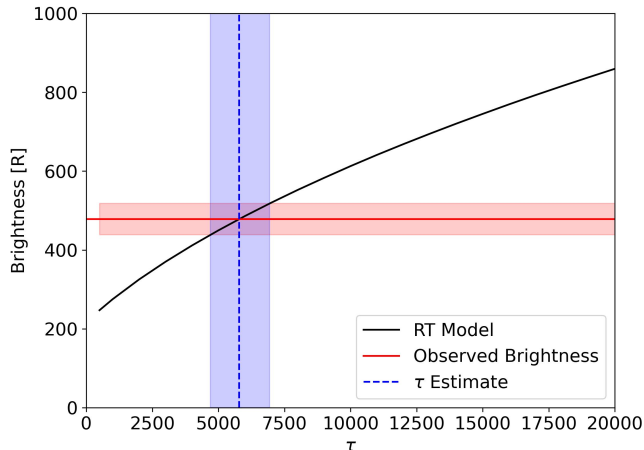


Figure 7. Retrieval of optical depth estimates (blue) by comparison of Cassini/UVIS observations (red) with the radiative transfer model (black) for a single pixel.

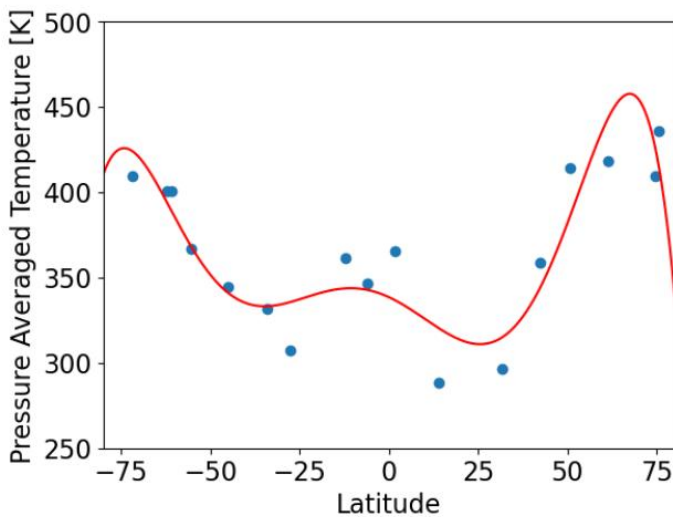


Figure 8. (blue) Pressure averaged temperatures above the methane homopause, from a 1D photochemical model (see Section 2.4), constrained by stellar UVIS occultations throughout 2017 (Brown et al. 2020). (red) The temperatures are fitted with a 6th order polynomial.

photoelectrons based on the reduced solar flux at Saturn and the emitting column of H at Saturn is approximately a factor 3 smaller than at Jupiter. Therefore, we expect photoelectron-induced Lyman α emissions to be negligible compared to scattered solar flux.

Recombination is a well known astrophysical source of Lyman- α emissions, and a possible source in hot exoplanet atmospheres. In cold planetary atmospheres, however, it is negligible. For H^+ recombination, we calculate the case-B recombination rate using H^+ and

e^- profiles from the 1D photochemical model (Moses et al. 2023), to estimate an upper limit for the production of excited H atoms ($n \geq 2$). Integrating this over the atmospheric column gives a column emission of only $\sim 10^{-3}$ R.

Observations of Lyman- α with high spectral resolution should be able to identify, or provide an upper limit on, a hot population of hydrogen in the atmosphere, such as HST/STIS echelle observations (see Fig. 3 in Ben-Jaffel et al. 2023). However, the uncertainties in the high-spectral resolution HST observations are significant, partly due to the subtraction of the strong geocoronal Lyman- α emission. Consequently, retrieving a useful upper limit on a hot atomic hydrogen population does not seem feasible. Ben-Jaffel et al. (2023) compare a reference and boosted (with 2-3 times the atomic hydrogen) photochemical model to the HST/STIS observations. The additional 280 R of emissions in the boosted model could similarly be attained by including a hot atomic hydrogen population ($\tau_{H,Hot} = 1$, $T_{Hot} = 25,000$ K), with minimal impact on the resulting lineshape. However, the mechanism for producing a significant suprathermal hydrogen population remains unclear.

One potential source of hot hydrogen in the upper atmosphere is recombination of H_3^+ , producing $H + H + H$ and $H + H_2$. We constrain this source by using the photochemical model profiles (Moses et al. 2023). At zeroth order, we assume local production of hot H (rates listed in Larsson et al. 2008) balanced by local cooling through elastic collisions of the hot H with thermal H and H_2 , with collision cross sections from Krstić & Schultz (1999). Under this assumption, the hot H population generated by recombination of H_3^+ in the upper atmosphere is negligible, with column densities a factor 10^7 smaller than the ambient atomic hydrogen column density. This hot H population is too small to generate Lyman- α emissions comparable to scattering by the thermal H population (a column of hot atoms a factor of 10^4 smaller than thermal H could generate similar emissions).

H_3^+ rain from the rings has been observed at Saturn (O’Donoghue et al. 2019). However, the ring rain latitudes show no obvious correlation with the observed Lyman- α bulge and it is difficult to anticipate a related mechanism that could generate enough hot atoms to explain the bulge. While we cannot rule out a hot population generated by another means, the observations and modelling at present appear most consistent with emissions driven by resonance scattering of solar flux by thermal atomic hydrogen.

2.4. Photochemical models of Saturn’s upper atmosphere

The upper atmospheric hydrogen is a probe of photochemistry deeper in the atmosphere, as it is primarily produced through photolysis of methane (Moses *et al.* 2000a), with only a small contribution from thermospheric chemistry. We compare the inferred H optical depths (outlined in Section 2.3) to two photochemical models: (a) 1D models tuned to the results of stellar occultations observed by Cassini/UVIS in 2016–2017 (Brown *et al.* 2020, 2024) and (b) a 2D model identical to Moses & Greathouse (2005), except we adopt solar-cycle average incident ultraviolet flux (including at Lyman- α), rather than tracking the ~ 11 year solar cycle variation from the recent era.

1D models—Throughout 2016 and 2017, stellar occultations provided a pole-to-pole map of the thermosphere (Brown *et al.* 2020) and were used to retrieve temperature profiles as well as the densities of many atmospheric constituents (e.g. H₂, CH₄ Brown *et al.* 2024). However, as we noted before, it is not possible to retrieve the H density profile from stellar occultations, due to absorption of starlight by the interstellar medium. The H density profile is calculated with the 1D photochemical model, constrained by the profiles of other molecules.

For this study, we are interested in the hydrogen and methane profiles, particularly the H column above the methane homopause. We consider optical depths of $\tau_{CH_4} = 1$ and $\tau_{CH_4} = 10$ at Lyman- α , using a cross-section of $1.79 \times 10^{-17} \text{ cm}^2$ (Chen & Wu 2004). For the purposes of the comparison between the inferred optical depths and the model, the H optical depth is integrated above the homopause altitude for each occultation location, in line with the pressure averaged temperatures above the homopause (see Figure 8).

2D model—We use the seasonally and meridionally varying 2D model of Moses & Greathouse (2005), which incorporates the time varying insolation to represent seasonal changes with solar-cycle averaged ultraviolet fluxes. In this model, the temperature-pressure profile is constant across latitudes and with season. It is important to note that this model parameterizes vertical transport by using an eddy diffusion profile that is constant with latitude and does not include any meridional transport. We integrate the H optical depth above the methane homopause ($\tau_{CH_4} = 1$) as a function of latitude and time (with the time mapped to the solar longitude; see Figure 9). At present, photochemical models that account for seasonal changes to the temperature structure and mixing rates in the middle and upper atmosphere do not exist. The differences between the inferred H column

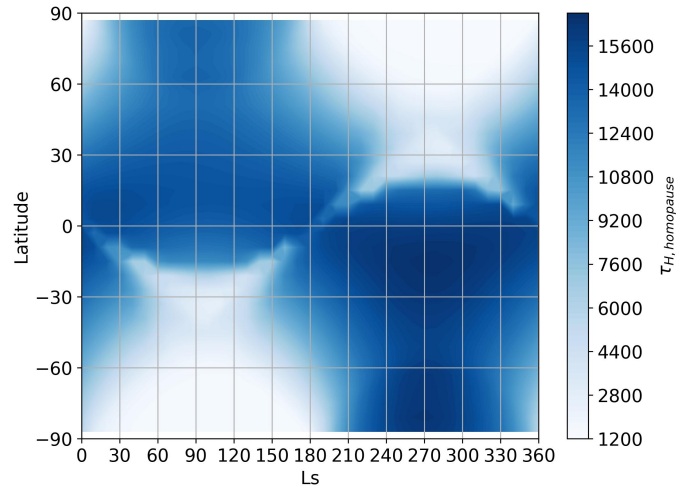


Figure 9. Optical depth of H above the methane homopause ($\tau_{CH_4} = 1$) from the 2D photochemical model, similar to Moses & Greathouse (2005). The x -axis is solar longitude with the northern solstice occurring at $L_S = 90^\circ$ and southern solstice at $L_S = 270^\circ$.

from the Lyman- α observations and the photochemical model predictions identified in this study represent the first step to guide the development of such models in the future.

3. RESULTS

3.1. A comparison of UVIS observations with the IPH model

In this section, we compare observations of the IPH Lyman- α background throughout 2006 with modelled IPH brightnesses (see Figures 10 and 11). The set of observations is listed in Table 3. The brightnesses of the IPH observations have been scaled to the solar flux on Jan 1st 2009, when the solar activity was at a minimum. This corrects for variation of the IPH that results from the Sun’s rotation. The scaled brightnesses are also given in Table 3. The modelled IPH brightnesses (black) agree well with the observations from Cassini/UVIS (blue), with an $R^2 = 0.64$. The brightness increases from 250 R in the anti-sunward direction ($\cos \theta_{Max} = -1$) to 650 R near the sunward direction ($\cos \theta_{Max} = 0.8$).

A cluster of 8 points at $\cos \theta_{Max} = 0.4$ with $B = 250 \pm 40$ R is 100 R smaller than predicted by the model. However, there are several observations at similar angles with $B = 450$ R, suggesting the IPH model is not overestimating the brightnesses at this angle. Overall, the IPH observations by Cassini are consistent with the predictions of the IPH model at a heliocentric distance of 9.1 au.

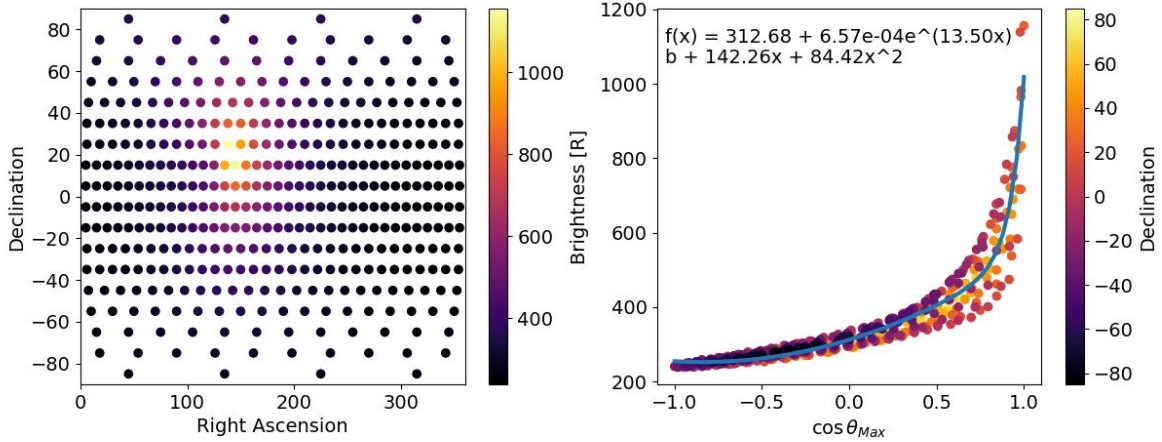


Figure 10. (left) Full sky map of the modelled IPH brightness at Saturn in 2006 (see Section 2.3.2). (right) Modelled IPH Lyman- α brightness against angle to direction of maximum brightness. The fit to the IPH brightness is shown in blue.

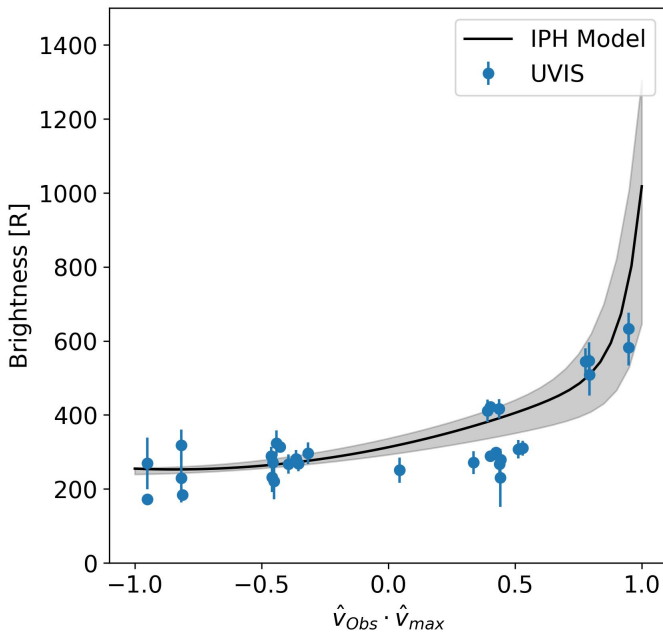


Figure 11. Comparison of IPH Lyman- α brightness from Cassini/UVIS observations throughout 2006 (blue) with the modelled brightness from the IPH background model (black, see Section 2.3.2 and Figure 10). The x axis is the cosine of the angle between the observation direction and direction of maximum brightness. The black line gives the best fit, with the shaded region depicting minimum and maximum modelled values.

3.2. Emission trends of Saturnian Lyman- α from multi-variate regression analysis

Figure 12 shows the predicted brightnesses vs the actual observed brightnesses of Lyman- α for the multi-variate regression model outlined in Section 2.2 for the testing dataset (20% of points). The coefficients of the fit to Eq. 1 are given in Table 1. The fit has an $R^2 = 0.791$

demonstrating that the observed brightness can be well parameterised by the latitude, incidence and emission angle once the observed brightness is scaled with the time-dependent solar flux. The 3-variable regression does not capture the brightnesses at small values, but above 250 R the model accurately predicts the observed brightnesses.

Figure 13 shows the dependence of the brightness on each of the independent variables around the constant values of $[\theta_{em}, \theta_{in}, \phi_{lat}] = [30, 30, 20]^\circ$ with the observed brightnesses shown for points within 10% of the constant values. The Lyman- α brightness is most strongly dependent on the incidence angle of light arriving from the Sun, with brightness decreasing strongly from the subsolar point ($\theta_{in} = 0$) to the terminator plane at $\theta_{in} = 90$. Conversely, the brightness increases with emission angle, with the brightest regions near the limb of Saturn’s disk. The dependence on the incidence angle closely fits a $\cos \theta_{in}$ dependence.

Figure 14a shows the radiation field predicted by the trained model at a latitude of 20°N , with the combined dependence of the brightness on the incidence and emission angles. It again demonstrates substantial darkening towards the terminator and brightening of the disk near the limb. The dependences of the observed brightness on latitude, emission and incidence angles are consistent when using different multi-variate regression models, such as support vector regression using radial basis fields.

In Figure 12b, there is non-linearity to the residuals, with a slight parabolic shape between 200 and 1000R. Beyond 1000 R, the MVR model overestimates the observed brightnesses, but the statistics at these values are much lower (< 150) compared to the intermediate brightnesses (200-1000 R). The structure in the residu-

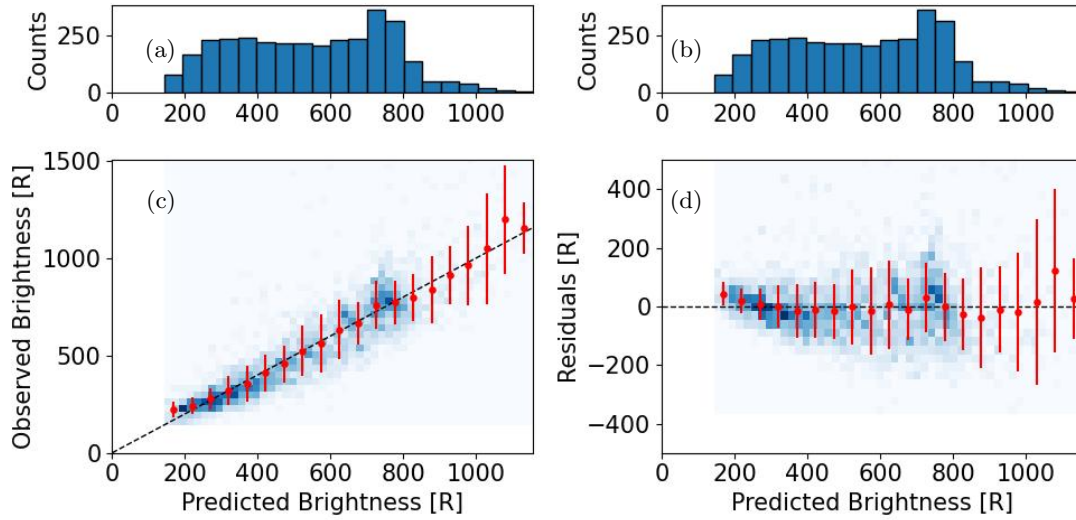


Figure 12. (a,b) Testing data counts vs predicted brightness from the MVR. (c) Observed brightnesses and (d) residuals vs predicted brightnesses for the testing dataset (blue) with the averages and standard deviations shown in red.

Emission Angle = 30, Incidence Angle = 30, Pixel Latitude = 20

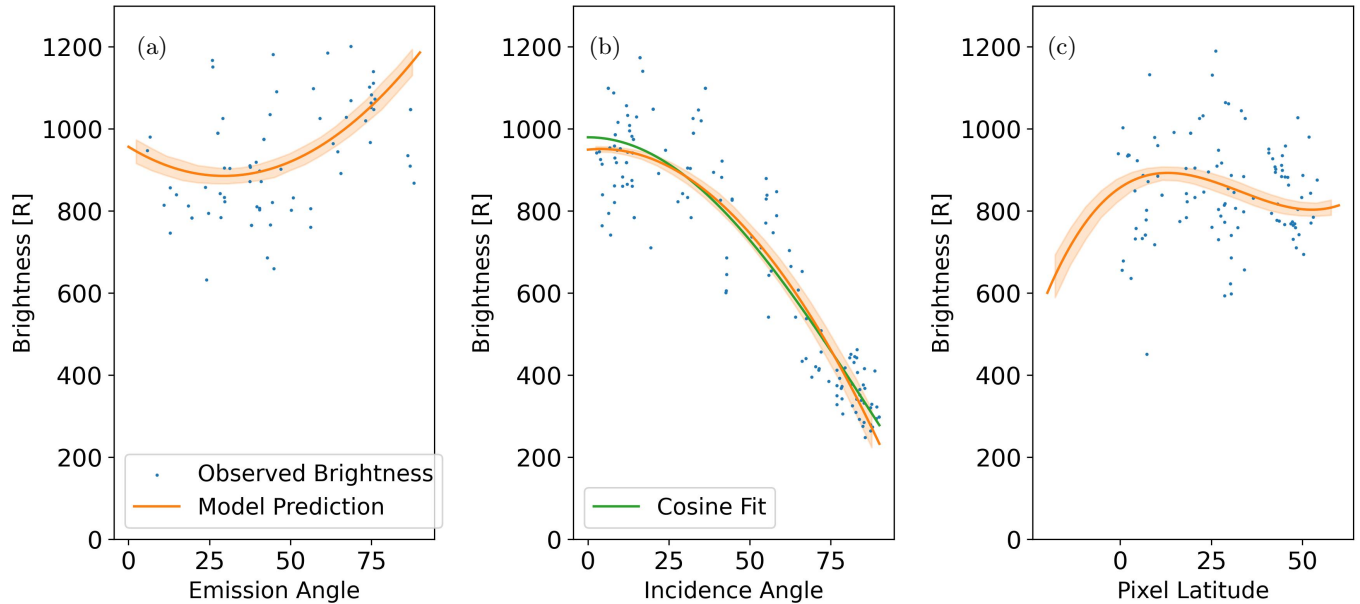


Figure 13. Comparison of the observed brightnesses from 2014-2016 in the testing dataset (blue) to the multi-variate regression predictions (orange) as a function of (a) emission angle, (b) solar incidence angle and (c) latitude. The observed data are within the intervals $\theta_{em} = [27, 33]$, $\theta_{in} = [27, 33]$ and $\phi_{Lat} = [18, 22]$ for the other two independent variables. In panel (b), the best fit of a cosine to the observed brightnesses is given (green).

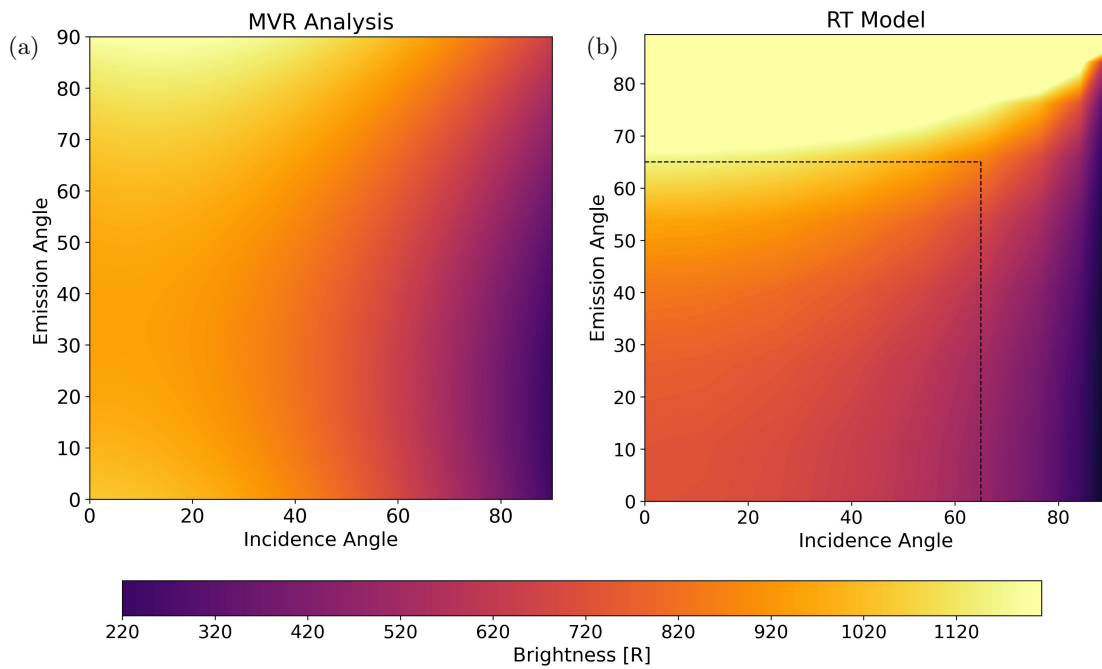


Figure 14. (a) Predicted brightness as a function of solar incidence and emission angles from the MVR analysis at a latitude of 20°N for the 2014-2016 dataset. (b) Modelled brightness as a function of solar incidence and emission angles from the radiative transfer model (see Section 2.3) for an optical depth of $\tau_H = 10000$ and $T_{Sat} = 350\text{ K}$. The dashed lines illustrate the region in which we compare observations to the radiative transfer model in Section 3.3.

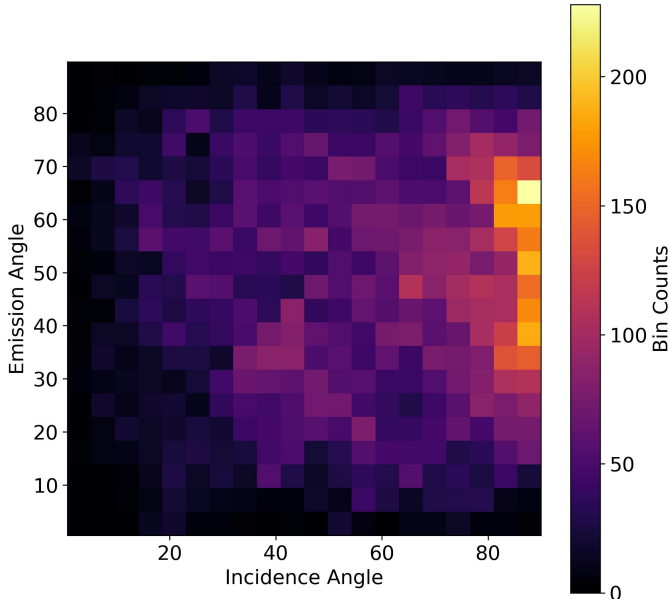


Figure 15. Histogram of observation geometries (solar incidence angles and emission angles) in the training dataset for the multi-variate regression from 2014-2016 (see Figures 13 and 14). Regions with fewer observations are less well constrained in the MVR model.

als is not replicated when considering the behaviour with respect to the independent variables (Figure 13). Each variable shows no discernable behaviour in the residuals, suggesting higher order terms for each variable are not required.

Figure 14b similarly shows the modelled brightness of Lyman- α from the radiative transfer model (Section 2.3) at a temperature of 350 K and an atomic Hydrogen optical depth of $\tau_H = 10,000$. The trained MVR model shows very similar behaviour to the brightness from the RT model, with a bright limb and dark terminator region, indicating that the observed brightnesses can be mostly explained by resonance scattering of Lyman- α by upper atmospheric atomic hydrogen. The MVR and RT model differ in two main areas: the bright limb of the RT model and the increase in brightness at low emission angles observed in the MVR model. The very bright limb observed in the RT model is a result of the plane-parallel assumption, which breaks down near the terminator and near the limb of the disk. With a plane parallel-model, the gas column the photons travel through is greatly overestimated, inflating the modelled brightness. The increase in brightness at low emission angles for the MVR may be a result of the limited data available at small emission angles (see Figure 15), which do not strongly constrain the observations at low emission and incidence angles.

The latitudinal variation seen in Figure 13c, has been disentangled from variation with the geometry of the observations without reliance on a radiative transfer model. The northern hemisphere bulge at low latitudes is a result of a meridional structure in the upper atmosphere. Using the same analysis for the 2004-2006 period, the latitudinal profile shows the reverse trend, with the bulge appearing near 20°S (see Figure 16). The brightness also decreases into the winter hemisphere and towards the summer pole. This shows a clear reversal with season in the latitudinal behaviour, and shows that the bulge is not a permanent feature of the northern hemisphere. Instead, it is a seasonally changing feature that appears in the summer or spring hemisphere.

The source of the increased brightness at 20° in the summer hemisphere could be driven by either enhanced H column in the region, or additional sources of emission within the bulge region. We split the dataset into latitude bins of 10° and applied the same multi-variate regression (see Figures 29 and 35). At all latitudes, the same dependence of the brightness on solar incidence and emission angles was observed, with $R^2 > 0.7$ and $R^2 > 0.6$ throughout northern and southern summers respectively. Some latitude bins were limited by the phase space coverage of the data (Figures 15, 36 and 30), with small emission angles not probed in the winter hemisphere or close to the poles. The consistency of the relation between the incidence and emission angles with latitude implies that there is not a substantial additional internal emission source in the northern hemisphere bulge. Therefore, the variation in Lyman- α brightness can likely be attributed to variation of the H column above the methane homopause. The alternative would be to attribute the variation to a seasonal change in the hot atomic H population, although no source of hot atoms that would have the required behaviour has been identified to date.

3.3. Seasonal Variation of Saturn's atmosphere

3.3.1. A case study of northern hemisphere summer

We consider first an observation of Saturn on 25th March 2016, when the subsolar latitude was 26.0°, with incidence and emission angles from 0 to 65°. We exclude latitudes poleward of 60°, and in the ring shadow region which extends from 14°S to the south pole. This includes 1617 pixels across the dayside region highlighted in Figure 17, accumulated over 4.5 hours. The observed brightness is constant between the latitudes of 0 and 20°N at 596 ± 15 R, before decreasing to 518 ± 12 R 26°N to 60°N. The observed brightness also drops sharply to 421 R at 9.4°S towards the ring-shadowed region (see Figure 18).

Emission Angle = 30, Incidence Angle = 30, Pixel Latitude = -20

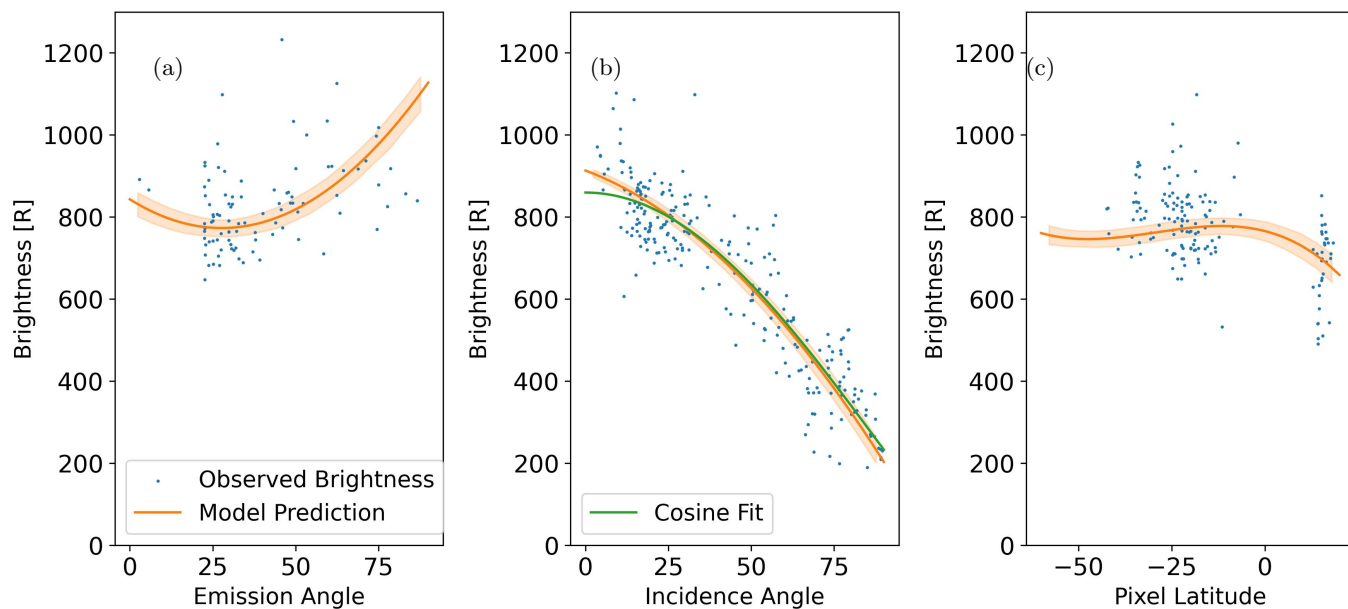


Figure 16. Comparison of the observed brightnesses in the 2004-2006 testing dataset (blue) to the multi-variate regression predictions (orange) as a function of (a) emission angle, (b) solar incidence angle and (c) latitude. The observed data are within the intervals $\theta_{em} = [27, 33]$, $\theta_{in} = [27, 33]$ and $\phi_{Lat} = [-22, -18]$ for the other two independent variables. In panel (b), the best fit of a cosine to the observed brightnesses is given (green).

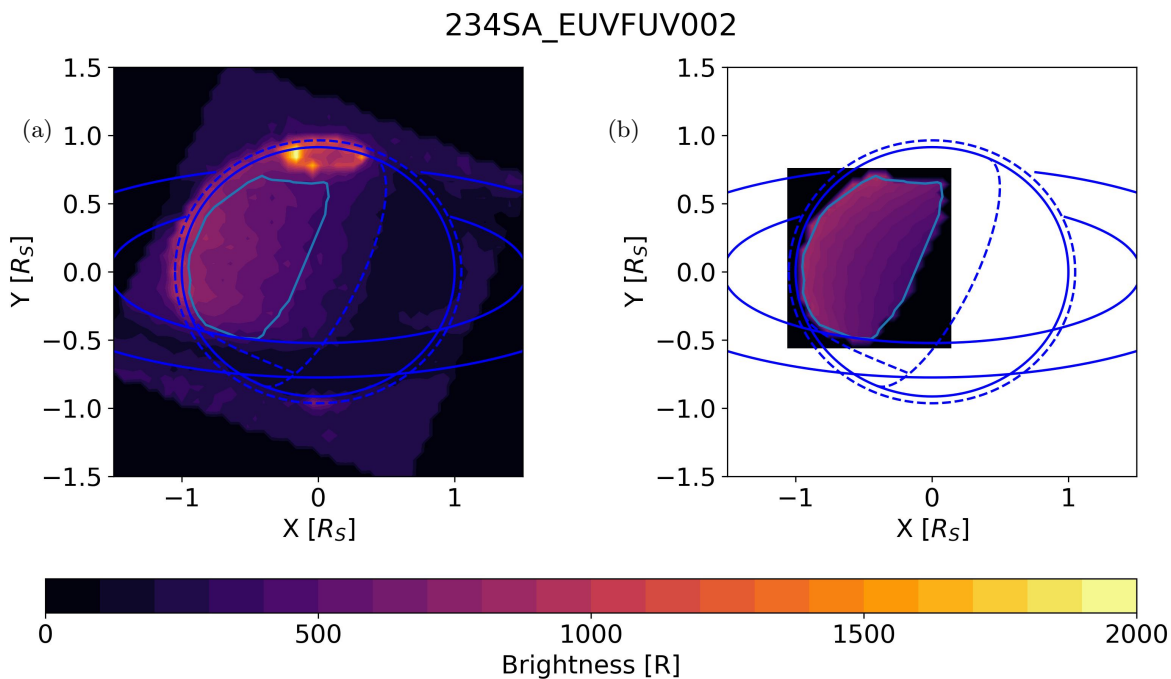


Figure 17. (a) Lyman- α brightness in observation 234SA_EUVFUV002, with the ring geometry, limb and terminator of Saturn highlighted in blue. The considered region for comparison to the radiative transfer model is bounded by the light blue line. (b) Modelled Lyman- α brightness using $\tau_H = 10,000$ and the temperature dependence in Fig. 8 in the RT model (see Section 2.3).

Table 1. Coefficients for the fit used in the multi-variate regression (see Eq. 1), for the 2014-2016 observations.

Variable	Coefficient	Mean Value	Confidence Interval
Constant	p_0	6.51×10^2	$(6.49 \times 10^2, 6.53 \times 10^2)$
θ_{em}	p_1	3.73×10^0	$(3.68 \times 10^0, 3.77 \times 10^0)$
θ_{in}	p_2	-1.01×10^1	$(-1.02 \times 10^1, -1.01 \times 10^1)$
ϕ_{lat}	p_3	-3.54×10^0	$(-3.64 \times 10^0, -3.44 \times 10^0)$
θ_{em}^2	p_4	7.95×10^{-2}	$(7.74 \times 10^{-2}, 8.17 \times 10^{-2})$
$\theta_{em} \cdot \theta_{in}$	p_5	3.05×10^{-2}	$(2.85 \times 10^{-2}, 3.25 \times 10^{-2})$
θ_{in}^2	p_6	-9.36×10^{-2}	$(-9.54 \times 10^{-2}, -9.17 \times 10^{-2})$
ϕ_{lat}^2	p_7	2.52×10^{-2}	$(2.25 \times 10^{-2}, 2.80 \times 10^{-2})$
ϕ_{lat}^3	p_8	2.55×10^{-3}	$(2.43 \times 10^{-3}, 2.66 \times 10^{-3})$

The modelled brightness for a constant H Lyman- α line center optical depth (hereafter, the H optical depth) of 10,000 also shown in Figure 18 agrees well with the brightness between 0 and 25°, but outside this range the modelled brightness increases in contrast to the observation. The increased brightness is a result of larger emission angles for the southern and higher latitudes. The scattered Lyman- α from the IPH background has a fairly constant contribution of 78.5 ± 4.4 R across latitudes, which is 12% of the brightness of the scattered solar flux.

Figure 18b shows the H optical depths retrieved from comparison of the observations with the RT model. The close agreement between the modelled and observed brightness between 0 and 25° is reflected by the constant optical depth of $10,800 \pm 300$ R over this range. Northward of 25°N the optical depth decreases continuously towards $\tau = 5000$ at 60°N, as the observed brightness declines relative to the expected values from the RT model based on constant H optical depth. This decrease in the H optical depth is not predicted by the 1D photochemical model, which predicts that the H optical depth is approximately constant at 10,000 up to 60°N. However, the 2D photochemical model (orange) does show a slight decrease in the H optical depth from the peak at 10°N, but only by 10%, compared to the 50% reduction retrieved from the UVIS data. Southward of the equator, the H optical depth sharply decreases between 5.6°N and 9.4°S latitude towards the ring shadow, in close agreement with the photochemical model.

3.3.2. A case study of southern hemisphere summer

Figures 19 and 20 show results for an observation from 8 Nov 2004, during southern hemisphere summer, with a subsolar latitude of 23.5°S. The spatial coverage of Saturn’s disk was much narrower for this case (see Figure 19), so the variation in the modelled brightnesses is much smaller at each latitude. The observed brightness decreases sharply from 1030 ± 38 R at 60°S to 780 ± 31 R at 40°S as a result of the decreasing emission angle. The lower brightness is closely matched by the modelled brightness based on constant H optical depth, and can be attributed wholly to changes in the viewing geometry.

The observations and constant H optical depth model, however, diverge between 40°S and the equator, with the modelled brightness continuing to decrease to 690 ± 7 R while the observed brightness increases to 888 ± 36 R in this region. The retrieved H optical depths (blue, Figure 20b) therefore increase substantially over this latitude range, peaking at $\tau_H = 17,500 \pm 2500$ at 13°S. Equatorward of the peak, the H optical depths decrease sharply towards the ring shadow region, closely mirroring the

behaviour observed in the northern hemisphere summer hemisphere (see Figure 18), and predicted by the 2D seasonal photochemical model (orange). The magnitude of the H optical depths in the summer hemisphere are also broadly consistent with the model, which predicts peak H optical depths of $\tau_H = 16,600$ at 3°S.

3.3.3. Implications for upper atmospheric hydrogen

Having examined two observations from the NH and SH summers, we now apply the same analysis to all the dayside disk observations from Cassini/UVIS from 2004 through to 2016. We exclude 2017 as there is little coverage of Lyman- α emissions from the dayside Saturn disk. We have calculated H optical depths for each pixel (as outlined in Section 2.3) and taken annual averages and standard deviations. We have separated the SH summer (2004-2006, Figure 21), equinox period (2007-2010, Figure 22) and NH summer periods (2011-2016, Figure 23).

Much like in the case study (Figure 20), the annual averages exhibit a substantial latitudinal variation during the southern summer (Figure 21), with H optical depths increasing from 60°S towards the hydrogen bulge in the SH between 10°S and 25°S. Northward of the bulge, the H optical depth declines sharply with latitude. There are few available observations north of 20°N throughout 2004-2006, as these latitudes are typically obscured by either the rings or the ring shadow region. The sharp decrease in H optical depth around the equator is also observed in the photochemical model. The decrease in the H optical depth at the equator is shifted southward relative to the photochemical model, and the gradient shifts southward from 2004 to 2006. This may result from the movement of the southern boundary of the ring shadow, which begins at 6.6-17.3°N in 2004 and reaches 4.4-12.3°N in 2006. The peak H optical depth, seen in the southern hemisphere bulge, decreases from 2004 to 2006. There is substantially more variation than expected based on the photochemical model (Moses & Greathouse 2005) and is discussed in Section 4.3.

During the equinox period (Figure 22), the H optical depths increase continuously from the polar regions at $\pm 60^\circ$ towards the equator. They agree well with the modelled depths from the 2D photochemical model (dash-dotted lines) in both magnitude and meridional structure. The equatorial latitudes have been excluded as they are obscured by the ring shadow and ring atmosphere during these years. The observed brightness decreases around the equator, but we cannot determine whether the H column is smaller due to the uncertainty in the illumination conditions. The H optical depths throughout this period show less variation than seen in the summer hemisphere (Figures 21 and 23), particu-

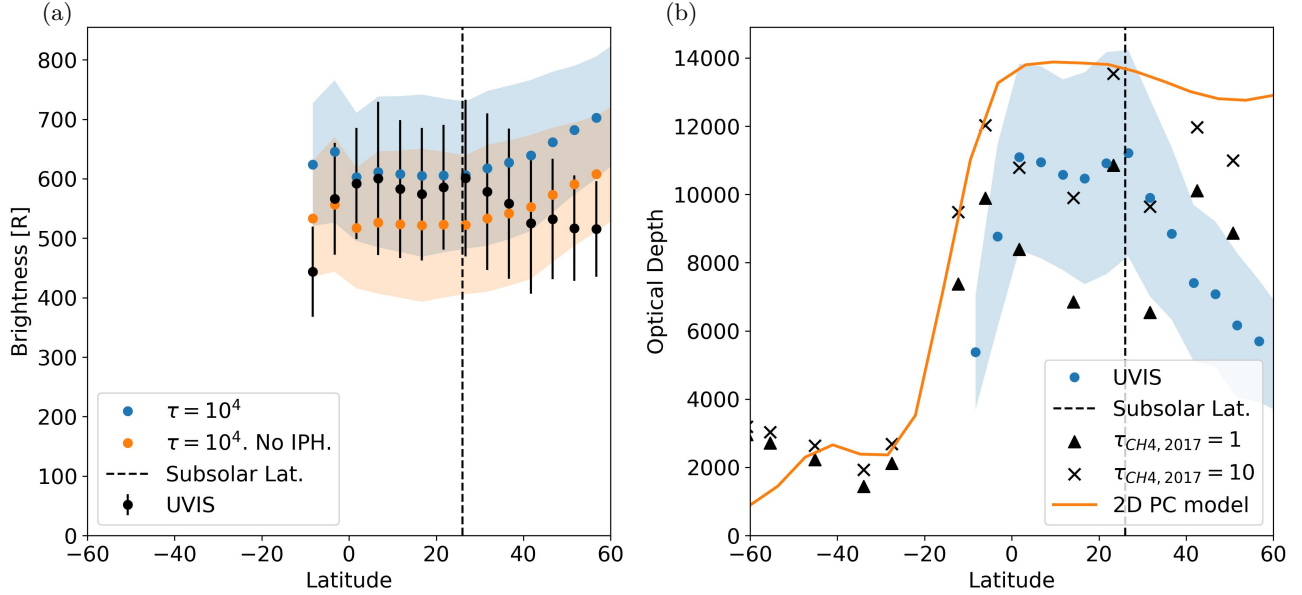


Figure 18. (a) Observed Lyman- α brightness (black) for observation 234SA_EUVFUV002 against latitude. The modelled brightness for the observation geometry using $\tau = 10000$ and the temperature variation in Fig.8 is shown with (blue) and without (orange) the contribution of scattered IPH Lyman- α . (b) Optical depth (blue) vs. latitude retrieved from comparison of Cassini/UVIS observations. The optical depths of the methane homopause (using $\tau_{CH_4} = 1$, triangles; and $\tau_{CH_4} = 10$, crosses) predicted by 1D photochemical models tuned to 2017 stellar occultations are shown. (orange) H optical depth from the 2D photochemical model on 26 Mar 2016 at subsolar latitude of 26.0° and $L_S = 81.2^\circ$ (see Figure 9).

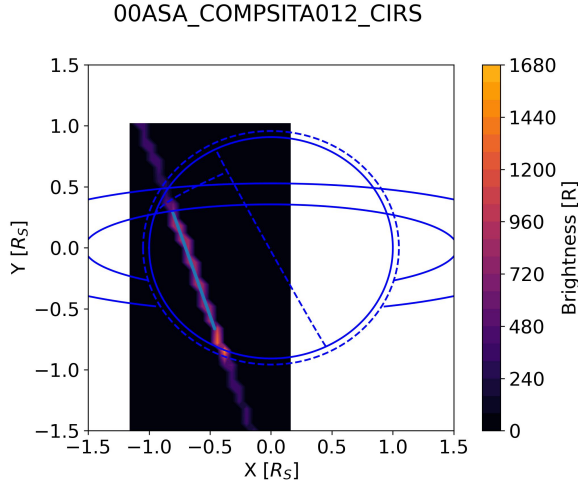


Figure 19. Observed Lyman- α brightness for the 00ASA_COMPSITA012_CIRS observation on 8 Nov 2004 with a subsolar latitude of -23.5° . The region modelled by the radiative transfer code is highlighted by the light blue line, with Saturn, the rings and ring shadow regions superimposed in dark blue.

larly in the northern hemisphere where the maximum H optical depth is $\tau_H = 17,200 \pm 2300$.

In the southern hemisphere during the equinox period, the peak H optical depths are similar, except in 2009 and 2010, which both exhibit significantly reduced

H optical depths at mid-latitudes. The lower brightnesses compared to 2007 and 2008 are unexpected, much like the substantial variation during the southern hemisphere summer. The retrieved H optical depths are also 40% smaller than the photochemical model predictions at $20^\circ S$. We note that the highest optical depths are not consistently located in the more illuminated hemisphere. While this is the case in 2007 and 2010, the optical depths in 2008 are largest in the northern hemisphere despite a subsolar latitude of $6^\circ S$.

During the northern summer (Figure 23), the hydrogen bulge has shifted from the southern hemisphere (Figure 21) to the northern hemisphere, along with the subsolar latitude. The H optical depth decreases continuously towards $60^\circ N$, as seen in the case study (Fig. 20). From 2011-2013, the southern hemisphere is not completely shadowed by Saturn's rings. The retrieved H optical depths are roughly constant at $\tau_H = 5000$ in the winter hemisphere and much smaller than the northern hemisphere peaks. This is also in good agreement with the 1D models based on 2017 stellar occultations (see Section 2.4), which predicted H optical depths of $\tau_H = 3000$ in the shadowed winter hemisphere. As seen during the earlier periods, there is substantial variability in the peak H optical depths over time. Large H optical depths of $\tau_H = 22,100 \pm 6990$ and $\tau_H = 24,000 \pm 6,200$ are observed in 2013 and 2014, while in 2012 and 2015

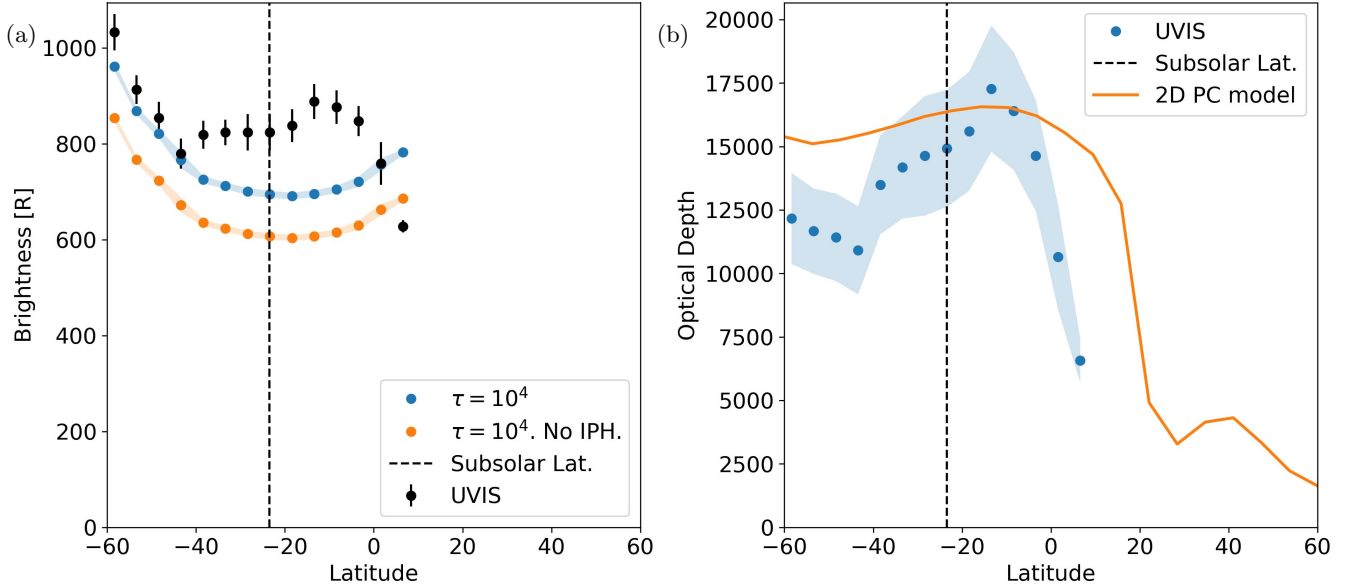


Figure 20. (a) Observed Lyman- α brightness (black) for observation 00ASA_COMPSITA012_CIRS against latitude. The modelled brightness for the observation geometry using $\tau = 10000$ and the temperature variation in Fig.8 is shown with (blue) and without (orange) the contribution of scattered IPH Lyman- α . (b) Optical depth (blue) vs. latitude retrieved from comparison of Cassini/UVIS observations with the radiative transfer model. (orange) H optical depth from the 2D photochemical model on 8 Nov 2004 at subsolar latitude of -23.5° and $L_S = 302^\circ$.

the peak H optical depths are $\tau_H = 10,000 \pm 4100$. The H optical retrieved from the observations in 2013 and 2014 are twice as large as those predicted by the 1D photochemical models and 50% larger than the predictions of the 2D model.

4. DISCUSSION

4.1. Source of Lyman- α emissions

The multivariate regression analysis of the Lyman- α brightness observations strongly supports the dominance of resonance scattering as the source of non-auroral Lyman- α emissions, with scattered solar flux comprising the majority of the observed emissions. The strong dependence of the Lyman- α brightness on the solar incidence angle (see Figure 13b) demonstrates the importance of solar photons in generating the observed emissions. Scattered photons from the IPH background would have a much weaker dependence on solar incidence angle, as they enter the atmosphere from all directions. Potential internal sources of Lyman- α photons would also not exhibit the variation with solar incidence angle, such as the electroglow proposed by (Shemansky et al. 2009) and others. While solar flux dominates, the contribution of scattered IPH Lyman- α photons is important for estimating of the H optical depth.

The radiation field retrieved through the multivariate regression analysis remains consistent across lati-

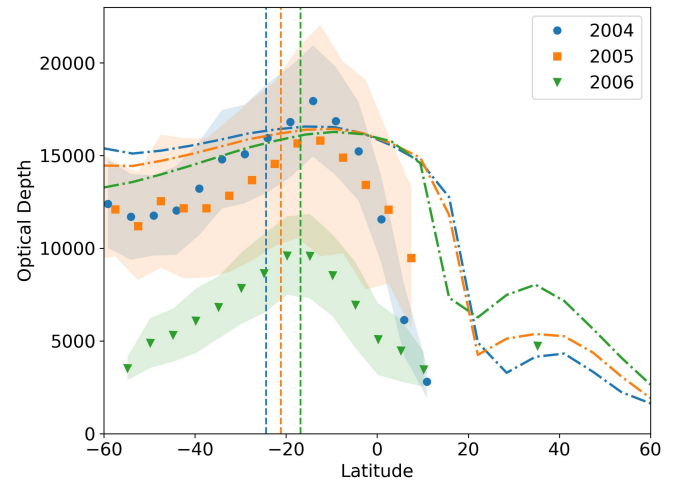


Figure 21. Yearly averages of the optical depths during the southern hemisphere summer (2004-2006) (colored circles), with shaded regions showing the uncertainty (see Section 2.3). The subsolar latitude for each year is given by the dashed vertical lines. The dash-dotted lines show τ_H predictions from the 2D photochemical model in each year.

tudes and mission periods. At all latitudes, the observed brightness can be fit with a quadratic function of incidence and emission angles, with brightness decreasing strongly towards larger incidence angles. For

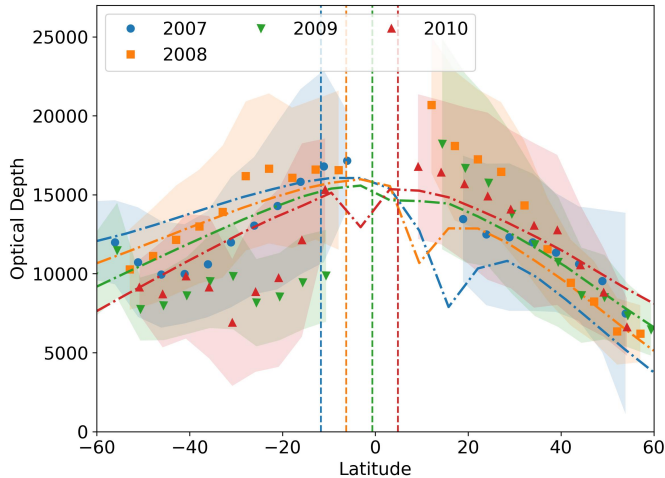


Figure 22. Yearly averages of the optical depths around equinox (2007-2010) (colored points), with shaded regions showing the uncertainty (see Section 2.3). The subsolar latitude for each year is given by the dashed vertical lines. The dash-dotted lines show τ_H predictions from the 2D photochemical model in each year.

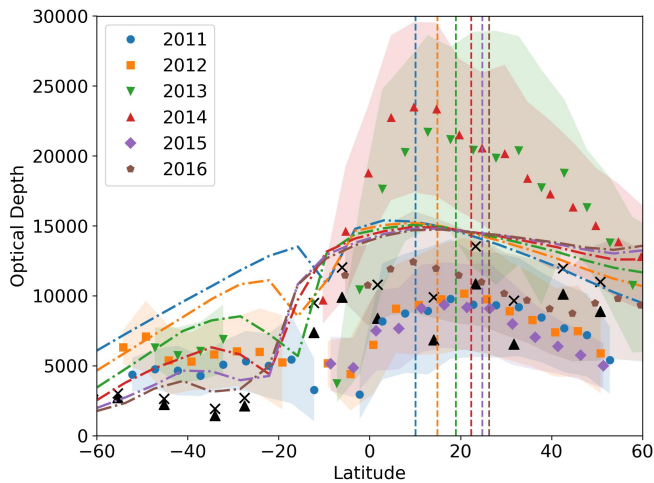


Figure 23. Yearly averages of the H optical depths during the northern hemisphere summer (2011-2016, colored points), with shaded regions showing the uncertainty (see Section 2.3). The subsolar latitude for each year is given by the dashed vertical lines, with the corresponding color. (black points) H optical depths above the methane homopause (at $\tau_{CH_4} = 1$, triangles; and $\tau_{CH_4} = 1$, crosses) from 1D photochemical models based on 2017 UVIS occultations (see Section 2.4). The dash-dotted lines show τ_H predictions from the 2D photochemical model in each year.

internal sources of emissions, we would not expect a strong dependence on solar incidence angle. The peak in the brightness and optical depth at latitudes of 10-20° in the summer hemisphere is therefore unlikely to

be driven by an internal emission source. Our results, however, do not discount the possibility of hydrogen or water entering the upper atmosphere from the rings in the equatorial region, such as that detected by INMS (Waite et al. 2018; Yelle et al. 2018; Serigano et al. 2020, 2022), and leading to local increases in the H density, although Cassini/UVIS occultations and photochemical modelling during the Grand Finale do not suggest that a substantial fraction of the influx materials vaporise in the thermosphere (Moses et al. 2023). A smaller suprathermal (25,000 K) hydrogen population (0.1% of the ambient H) could drive substantial emissions. The existence of such a population is currently hypothetical but can be better constrained with detailed modelling of emission profiles from Saturn's limb. Assuming no hot hydrogen population, the τ_H variation is similar to that predicted by the 2D photochemical model, which predicts a sharp decrease in the H column in the winter hemisphere (see Fig 9). This strongly suggests that the low-latitude brightness peak is seasonal in nature and origin.

4.2. The IPH model and Cassini/UVIS calibration

The brightnesses predicted by our IPH model (Section 2.3.2) agree well in both viewing direction and magnitude with observations of the IPH Lyman- α emissions by Cassini/UVIS (see Figure 11).

A proposed recalibration of Cassini/UVIS at Lyman- α by a factor 1.7 (Ben-Jaffel et al. 2023; Pryor et al. 2024) would result in much larger observed brightnesses for the IPH (1255 R at $\cos \theta_{Max} = 0.94$) compared to those predicted by the IPH model (762 R). This would require a significant increase in the hydrogen density at the termination shock, or galactic emissions beyond the scale of current estimates (Gladstone et al. 2021). The angular dependence of the disparity could not be rectified by additional galactic Lyman- α flux. We note that Ben-Jaffel et al. (2023) obtained the calibration factor by comparing Cassini/UVIS observations with Saturn disk brightnesses observed by HST/STIS in 2017 from Earth orbit. There were, however, no simultaneous dayside observations of Saturn's disk obtained by Cassini/UVIS in 2017 and the comparison also depends on viewing geometry as indicated here. The required corrections for IPH absorption and geocorona also make it difficult to extract the line shape from HST/STIS observations.

Our IPH model, which is constrained by observations of New Horizons Alice and SWAN/SOHO (Quémérais et al. 2013a; Izmodenov et al. 2013), predicts the brightness of the IPH Lyman- α to reach 250 R in the anti-sunward direction during the 2006 observations and rise to 900 R in the sunward direction. SWAN/SOHO was

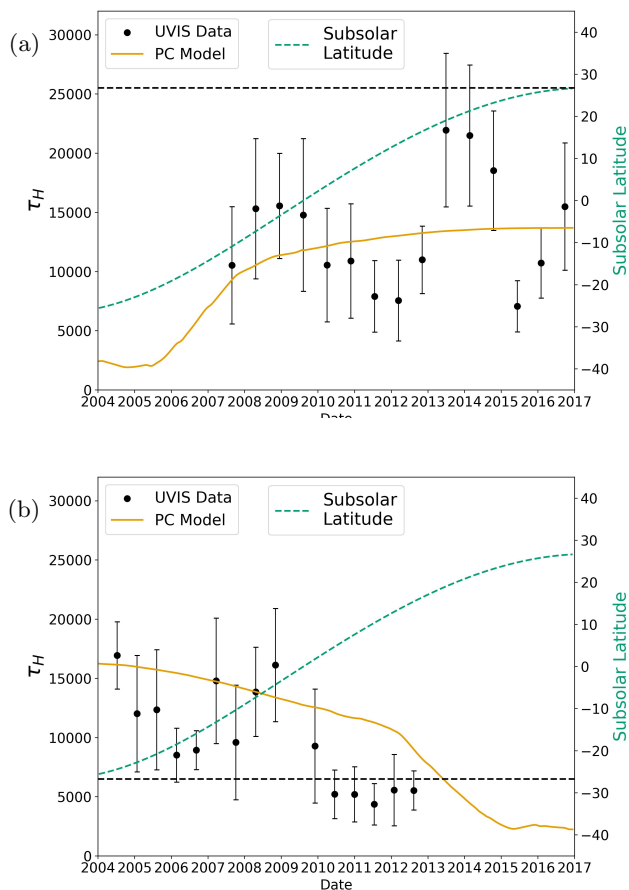


Figure 24. (a) Optical depth at $26.7^{\circ}\text{N}\pm 5$ (northern solstice latitude, black dashed line), throughout the Cassini mission from the (black) UVIS observations and RT model comparison (see Section 2.3) and (orange) the 2D photochemical model (see Section 2.4). The subsolar latitude is shown in green. (b) The same as above but for -26.7° (southern solstice latitude). The large error bars from the UVIS retrieval reflect shorter term variability in the Lyman- α brightness and atomic hydrogen atmosphere, within each temporal bin. The trends in the optical depths shown here demonstrate the long timescale variation of the atmosphere.

cross-calibrated with HST/STIS in 2001, and later observations in March 2023 show the instruments agree within 15%. (Qu  merais et al. 2013a). The good agreement between the model and UVIS observations suggests that the calibrations of Cassini/UVIS and the other instruments are consistent, although we cannot discount the possibility of recalibration by up to 20%.

4.3. Seasonal variability in thermospheric atomic hydrogen

Assuming that a population of hot atoms is not significant, the H optical depths retrieved from the UVIS observations with the RT model (see Section 3.3) agree well with the optical depths predicted by the photochemical model. The peak in brightness, identified in the northern hemisphere by Ben-Jaffel et al. (2023), translates to an increase in the atomic hydrogen optical depth above the methane homopause. However, the bulge at 20°N is not a permanent feature of the northern hemisphere, but shifts with season and is observed in the southern hemisphere during the southern summer (see Figure 21). A similar peak in the H optical depth is also predicted by the 2D photochemical model, which clearly shows a reversal in season (see Figure 9).

The poleward decrease in H optical depth from 20° to 60°N in northern summer is also predicted by the 2D photochemical model (Figure 9), although not to the same extent as estimated by the UVIS/RT model comparison. The poleward decrease disagrees with the 1D photochemical models, which were tuned to stellar occultations in 2017 (black points, Figure 23; Brown et al. 2024). These models do not show a significant decrease in the H optical depth towards higher latitudes, and also do not exhibit the same bulge around 20°N . The magnitude of the H optical depths is consistent with the results of the photochemical models (both 1D and 2D) with typical optical depths between $\tau_H = 5,000\text{--}15,000$ (see Figures 9, 20, and 23). The proposed revision of the Cassini/UVIS sensitivity by Ben-Jaffel et al. (2023), increasing observed Lyman- α brightnesses by a factor 1.7, would result in more significant enhancements in the retrieved optical depths. While the latitudinal and seasonal trends would be unaffected, the non-linear relationship between optical depth and brightness (see Figure 3) would see an increase of 2.5 to $3\times$ in the H optical depth compared to the current estimates. As a result, the retrieved hydrogen column densities would be inconsistent with either the 1D or 2D photochemical models, albeit at the same time roughly following the seasonal behaviour predicted by the models.

The proposed calibration factor means that an additional emission source or an alternative source of H would be required. The strong dependence of brightness on solar incidence angle, identified in the multivariate regression (see Section 3.2), excludes an emission source of the required magnitude other than resonance scattering of solar flux. While an additional source of hydrogen is not excluded by the current analysis, the magnitude of atomic H required would be beyond the estimates of what is possible from equatorial ring inflow (up to $1.75\times$, Ben-Jaffel et al. 2023), and would be required planet-wide. Photochemical modelling suggests

that ring rain entering the atmosphere as solid particles is unlikely to vaporize and contribute to the background gaseous atmosphere, and therefore should not significantly enhance the H column. A smaller population of hot H in the thermosphere is not excluded by our analysis but remains unidentified.

The year-to-year variability of the optical depths retrieved, however, is highly unexpected, with variation by a factor 2 observed from one year to the next (see Figure 24). The 2D photochemical model (orange), which incorporates the variation of the subsolar latitude but neglects EUV solar-cycle variation, predicts minimal short-term variation of the H column above the homopause. Between solar minimum and maximum, a variation by about a factor of 2 is expected in the H column (Ben-Jaffel et al. 2023), but on the shorter timescales of the observed behaviour, the variability of the H optical depth is far greater than expected.

To illustrate the variability, Figure 24a shows the optical depth at $26.7 \pm 5^\circ\text{N}$ and Figure 24b for $26.7 \pm 5^\circ\text{S}$, the subsolar latitudes of the northern and southern hemisphere solstices. At $26.7 \pm 5^\circ\text{S}$, the 2D photochemical model predicts a continuous and monotonic reduction in the H optical depth above the methane homopause from 2004 to the end of mission in 2017, while the reverse is true for the northern hemisphere.

The retrieved H optical depths from Cassini/UVIS show the same overall trend with time for $\phi_{lat} = 26.7^\circ\text{S}$, initially large at values of $\tau_H = 18,000$ and subsequently decreasing into the NH summer, when the ring shadows much of the southern hemisphere. However, the optical depth appears to oscillate around a mean value similar to the photochemical model. The trend is repeated in the northern hemisphere, with a sinusoidal time dependence around the photochemical model average. This indicates that there may be additional time-dependent behaviour that is modifying the upper atmospheric hydrogen content with a timescale of several years. The source of this time-variability is not incorporated into the photochemical model and requires further investigation.

The solar cycle is a natural candidate for this temporal dependence, which was at a minimum in 2009 and peaked in 2013 and 2014 (see Figure 4). The variation of the UV flux could modulate chemistry (e.g. methane photolysis) and temperature profiles in the thermosphere leading, which in turn would impact the upper atmospheric hydrogen. While some years could be explained by this process (e.g. large optical depths in 2014, Figure 23), the variation of the thermospheric hydrogen often bucks trends with the solar cycle (e.g.

2015 vs 2016). As such, there is likely an alternative or additional driver of changes in the thermosphere.

One possible source of the variation in the inferred H optical depths could be changes in the thermospheric temperature. The 2D seasonal photochemical model does not include temperature changes with either season or latitude. Occultations and circulation models have shown that thermospheric temperatures vary both seasonally and meridionally (Müller-Wodarg et al. 2019; Brown et al. 2020; Koskinen et al. 2021). Increases in thermospheric temperatures lead to increases in the scale height and the brightness from resonant scattering of solar flux. The factor of two variation in the inferred optical depth (see Figure 24) could be reconciled by a 40% temperature change (i.e., 350 K to 500 K), for the same density of H above the methane homopause. For example, a temperature variation of the order of 150 K between 2006 and 2017, with a peak temperature around 2010-2012, has been observed in the middle thermosphere around the equator in the UV occultation data (Koskinen et al. 2021). In addition, the homopause depth likely changes over time, due to the effect of the changing seasons on dynamics in the middle atmosphere. For example, downwelling near the homopause would drive methane deeper in the atmosphere and increase optical depths. Disentangling the possible drivers of atomic hydrogen variability will require a seasonal model in which the temperature structure and homopause depth also change with time, combined with an analysis of the occultations, H₂ emission data, and limb scans from the duration of the Cassini orbital mission. We note that the analysis of solar occultations and limb scans can be used to retrieve vertical profiles of H and therefore further constrain additional degradation of the Cassini/UVIS instrument and calibration at Lyman- α .

5. CONCLUSION

We have examined the extensive dataset of Lyman- α emissions from the Saturn disk throughout the Cassini mission, as well as observations of Lyman- α emitted from the interplanetary hydrogen background. We compared the IPH Lyman- α observations with the model of Quémerais et al. (2013a), which is calibrated with observations from SWAN, New Horizons Alice, and other platforms (Quémerais et al. 2013a; Izmodenov et al. 2013). The Cassini/UVIS observations and the IPH model agree well with each other, suggesting that the calibration of Cassini/UVIS at Lyman- α is consistent with the instruments underlying the IPH model.

We applied a multi-variate regression analysis to the observed brightness throughout the mission, to disentangle variations as a result of observation geometry and

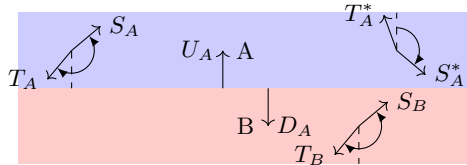


Figure 25. Diagram of layers A and B, with optical depths τ_A and τ_B . Upward ($U_{A,B}$) and downward fluxes for each layer are shown, in addition to the scattering ($S_{A,B}$) and transmission functions ($T_{A,B}$). Starred variables are oriented opposite to the typical direction and are important for multiple scattering.

those from meridional changes in the atmosphere. The emission brightness from Saturn’s disk is dependent on four key variables: solar flux at the top of the atmosphere, latitude, and the emission and incidence angles applicable to the observations. The dependence of the observed Lyman- α brightness on the emission and incidence angles agrees closely with a model of resonant scattering of solar photons, exhibiting a strong decrease of the observed brightness with increasing solar incidence angle. We therefore exclude the possibility of a substantial internal source of Lyman- α emissions outside auroral regions.

We observe a bulge in the Lyman- α emissions in both the northern and southern hemispheres, during their respective summer seasons. Therefore, we conclude that the bulge previously reported by Ben-Jaffel et al. (2023) in the northern hemisphere during spring and summer is a seasonally modulated feature. Around the equinox, the Lyman- α brightness and effective H optical depths increase towards the equator (once the ring and ring shadow are excluded) in both hemispheres, giving the equatorial region an appearance of a bulge.

We compared observations of Lyman- α emissions taken during the Cassini orbital mission to a radiative transfer model, using the model to retrieve estimates of the H optical depth above the strongly-absorbing methane homopause level. The magnitude and latitudinal variation of the H column agree well with the predictions of the photochemical model (2D in particular), albeit with much more substantial temporal variability in the observations. A comparison of the temporal changes in the southern and northern hemispheres again show further evidence of seasonal change in the upper atmospheric hydrogen, with a peak in the effective H optical depths at a latitude of 20° in the summer hemisphere.

The atomic H column decreases sharply into the winter hemisphere towards the ring shadow and more gradually toward higher latitudes (60°). While the seasonal photochemical model of Moses & Greathouse (2005) predicts roughly constant peak optical depths of $\tau_H = 15,000$ with season, our peak optical depth estimates varied by up to a factor 2 year-to-year. At latitudes of $\pm 26.7^\circ$, the optical depth appears to show a sinusoidal variation in time around the mean depth of the photochemical model, especially in the northern hemisphere. The source of this variation requires further examination.

Observations of emissions from the limb and terminator of the planet have been avoided in this study due to the plane-parallel assumption used in the radiative transfer model. Further work is required to analyse the limb and near-limb observations, which would provide a constraint on the vertical profile of the atomic hydrogen in the thermosphere. This would provide much greater constraints on the possibility of a suprathermal hydrogen layer in the upper atmosphere than nadir scans that probe scattering by the bulk of the H column. Additionally, the Lyman and Werner bands of H_2 and He 584Å line emission should also be addressed to infer constraints on energy deposition as well as the H_2 and He densities in the upper atmosphere.

ACKNOWLEDGMENTS

PS, TTK and JM acknowledge support by the NASA Cassini Data Analysis Program grant 80NSSC22K0306. ZB acknowledges support by the NASA/CDAP grant 80NSSC19K0902. PL acknowledges support from the project ATMHAZE within the framework of the CNRS-UArizona collaboration initiative Searching for Habitable Worlds, in the Solar System and Beyond.

APPENDIX

A. RADIATIVE TRANSFER MODEL

The radiative transfer model is a plane-parallel model based on iterative doubling and adding of layers. Two layers of the atmosphere, A and B with A above B (see Figure 25), are combined with

$$U_A = S_B \exp \left[-\tau_A \frac{\psi(x_{in}) + \bar{\omega}_a}{\mu_{in}} \right] + S_B \cdot D_A \quad (\text{A1})$$

$$D_A = T_A + S_A^* \cdot U_A \quad (\text{A2})$$

$$S_{A+B} = S_A + \exp \left[-\tau_A \frac{\psi(x_{em}) + \bar{\omega}_a}{\mu_{em}} \right] U_A + T_A^* \cdot U_A \quad (\text{A3})$$

$$T_{A+B} = \exp \left[-\tau_A \frac{\psi(x_{in}) + \bar{\omega}_a}{\mu_{in}} \right] T_B +$$

$$D_A \exp \left[-\tau_B \frac{\psi(x_{em}) + \bar{\omega}_a}{\mu_{em}} \right] + T_B \cdot D_A \quad (\text{A4})$$

where

- $U, D = U, D(x_{em}, \theta_{em}, \phi_{em}; x_{in}, \theta_{in}, \phi_{in})$ are the upward and downward fluxes at the layer boundaries.
- x_{em}, x_{in} are the emitted and incident frequency
- θ, θ_0 are the angles of emission and incidence, with $\mu = \cos \theta$.
- τ is the optical depth of a layer
- S and $T = S, T(\tau; x_{em}, \theta_{em}, \phi_{em}; x_{in}, \theta_{in}, \phi_{in})$ are the scattering and transmission functions for each layer with the starred values indicating they are defined opposite to the typical direction (scattering is typically upwards, transmission downwards).
- $\psi(x)$ is the Lyman- α lineshape, characterised by a Voigt profile at the upper atmospheric temperature
- $\bar{\omega}_a$ is the absorption albedo, which has been set to 0 throughout

We note that Equations A2 and A3 differ slightly from Equations 8 and 9 in Yelle et al. (1989), as we more explicitly define the directions of the scattering function. The final term in Eq. 10 of Yelle et al. (1989) is a typo and is corrected in Equation A4.

The dot product is defined as

$$S_A \cdot U_A = \frac{1}{4\pi\mu} \int_0^{2\pi} d\phi' \int_0^1 d\mu' \int_{-\infty}^{\infty} dx' \left\{ S_A(\tau_A; \mathbf{x}_{em}; \mathbf{x}') U_A(\tau_A; \mathbf{x}'; \mathbf{x}_{in}) \right\} \quad (\text{A5})$$

where the vectors $\mathbf{x} = (x, \mu, \phi)$ for each set.

The brightness of scattered solar flux is given by

$$4\pi I_{Sol}(\mu_{em}, \mu_{in})[R] = \Delta\nu_{D,Sat} \times 10^{-6} \times \int_{-\infty}^{\infty} dx_{in} \int_{-\infty}^{\infty} dx_{em} S(\tau; \mathbf{x}_{em}; \mathbf{x}_{in}) F_{Sol}(x_{in}) \quad (\text{A6})$$

where F_{Sol} is the solar Lyman- α flux incident on the atmosphere, with an incidence angle of θ_{in} . The Doppler width in Saturn's thermosphere is

$$\Delta\nu_{D,Sat} = \frac{\nu_0 v_{th}}{c} = \frac{\nu_0}{c} \sqrt{\frac{2k_B T_{Sat}}{m}}. \quad (\text{A7})$$

B. THIN LAYER APPROXIMATIONS

From Yelle (1988), we have the equation for the scattering function, S :

$$\begin{aligned}
\left[\frac{\psi(x_{em})}{\mu_{em}} + \frac{\psi(x_{in})}{\mu_{in}} \right] S(\tau; \mathbf{x}_{em}; \mathbf{x}_{in}) + \frac{\partial S(\tau; \mathbf{x}_{em}; \mathbf{x}_{in})}{\partial \tau} = \\
R(\tau; \mathbf{x}_{em}; \mathbf{x}_{in}) + \frac{1}{4\pi} \int_0^{2\pi} d\phi' \int_0^1 \frac{d\mu'}{\mu'} \int_{-\infty}^{\infty} dx' \left\{ \right. \\
R(\tau; \mathbf{x}_{em}; x', \mu', \phi') S(\tau; x', \mu', \phi'; \mathbf{x}_{in}) \left. \right\} \\
+ \frac{1}{4\pi} \int_0^{2\pi} d\phi' \int_0^1 \frac{d\mu'}{\mu'} \int_{-\infty}^{\infty} dx' \left\{ \right. \\
S(\tau; \mathbf{x}_{em}; x', \mu', \phi') R(\tau; x', \mu', \phi'; \mathbf{x}_{in}) \left. \right\} \\
+ \frac{1}{16\pi^2} \int_0^{2\pi} d\phi' \int_0^1 \frac{d\mu'}{\mu'} \int_{-\infty}^{\infty} dx' \int_0^{2\pi} d\phi'' \int_0^1 \frac{d\mu''}{\mu''} \int_{-\infty}^{\infty} dx'' \left\{ \right. \\
S(\tau; \mathbf{x}_{em}; x', \mu', \phi') \\
\left. \times R(\tau; x', -\mu', \phi'; x'', \mu'', \phi'') S(\tau; x'', \mu'', \phi''; \mathbf{x}_{in}) \right\} \quad (B8)
\end{aligned}$$

with

- $\mathbf{x}_{in} = (x_{in}, \mu_{in}, \phi_{in})$ and \mathbf{x}_{em} is the corresponding vector for the emitted flux
- $x_{in,em}$ are the incident and emitted frequencies
- $\mu_{in,em} = \cos \theta_{in,em}$ with incidence and emission angles $\theta_{in,em}$
- $\phi_{in,em}$ are the azimuthal incidence and emission angles
- τ - optical depth of the layer at the line centre
- $\psi(x)$ - line shape as a function of frequency
- S is the scattering function of the incident flux from $(x_{in}, \mu_{in}, \phi_{in})$ to $(x_{em}, \mu_{em}, \phi_{em})$ by the layer of thickness τ
- R is the angular dependent partial frequency redistribution function R_{II} from Hummer (1962).

Neglect the multiple scattering terms as we consider a thin layer and set

$$\eta = \frac{\psi(x_{em})}{\mu_{em}} + \frac{\psi(x_{in})}{\mu_{in}} \quad (B9)$$

An integration factor of $\exp(\eta\tau)$ gives

$$\frac{\partial (S(\tau, x_{em}, \mu_{em}, \phi_{em}, x_{in}, \mu_{in}, \phi_{in}) \exp(\eta\tau))}{\partial \tau} = R(\tau, x_{em}, \mu_{em}, x_{in}, \mu_{in}) \exp(\eta\tau) \quad (B10)$$

Integrating from zero to optical depth τ and simplifying we get:

$$S(\tau; \mathbf{x}_{em}; \mathbf{x}_{in}) = \frac{R(\tau; \mathbf{x}_{em}; \mathbf{x}_{in})}{\eta} [1 - \exp(-\eta\tau)] \quad (B11)$$

This is then expanded using a MacLaurin series and using $a = \eta\tau$ to get

$$S(\tau; \mathbf{x}_{em}; \mathbf{x}_{in}) = \frac{R(\tau; \mathbf{x}_{em}; \mathbf{x}_{in})\tau}{a} \sum_{n=1}^{\infty} \frac{(-a)^n}{n!} \quad (\text{B12})$$

Expanding this to 8th order gives the thin layer approximation:

$$S(\tau; \mathbf{x}_{em}; \mathbf{x}_{in}) = R(\tau; \mathbf{x}_{em}; \mathbf{x}_{in})\tau \left(1 - a \left(1 - \frac{a}{2} \left(1 - \frac{a}{3} \left(1 - \frac{a}{4} \left(1 - \frac{a}{5} \left(1 - \frac{a}{6} \left(1 - \frac{a}{7} \left(1 - \frac{a}{8} \right)\right)\right)\right)\right)\right)\right)\right) \quad (\text{B13})$$

For the thin layer transmission function, T , the equation of transfer is:

$$\frac{\psi(x_{in})}{\mu_{in}} T(\tau; \mathbf{x}_{em}; \mathbf{x}_{in}) + \frac{\partial T(\tau; \mathbf{x}_{em}; \mathbf{x}_{in})}{\partial \tau} = \exp\left(-\tau \frac{\psi(x_{em})}{\mu}\right) R(\mathbf{x}_{em}; \mathbf{x}_{in}) + \dots \quad (\text{B14})$$

Setting $\alpha = \frac{\psi(x_{in})}{\mu_{in}}$ and $\beta = \frac{\psi(x_{em})}{\mu_{em}}$ and using an integrating factor of $\exp(\alpha\tau)$ gives

$$T = R \frac{1}{\beta - \alpha} [\exp(-\alpha\tau) - \exp(-\beta\tau)] \quad \text{if } \alpha \neq \beta \quad (\text{B15})$$

To get the thin layer approximation expand both of the exponentials and use $a = \alpha\tau$ and $b = \beta\tau$

$$T = R\tau(b-a)^{-1} \left[1 - a + \frac{a^2}{2!} - \frac{a^3}{3!} + \frac{a^4}{4!} + \dots\right] \quad (\text{B16})$$

$$\left[-1 + b - \frac{b^2}{2!} + \frac{b^3}{3!} - \frac{b^4}{4!} + \dots\right] \quad (\text{B17})$$

Reorganising these terms gives the expression

$$T = R\tau \left[c_1 - \frac{1}{2} \left(c_2 - \frac{1}{3} \left(c_3 - \frac{1}{4} \left(c_4 - \frac{1}{5} \left(c_5 - \frac{1}{6} \left(c_6 - \frac{1}{7} \left(c_7 - \frac{c_8}{8} \right)\right)\right)\right)\right)\right)\right] \quad (\text{B18})$$

where

$$c_1 = 1 \quad (\text{B19})$$

$$c_2 = a + b \quad (\text{B20})$$

$$c_3 = a^2 + ab + b^2 \quad (\text{B21})$$

$$c_4 = (a^2 + b^2) \times c_2 \quad (\text{B22})$$

$$c_5 = a^4 + a^3b + b^2a^2 + ab^3 + b^4 \quad (\text{B23})$$

$$c_6 = (a^3 + b^3) \times c_3 \quad (\text{B24})$$

$$c_7 = a^6 + a^5b + a^4b^2 + a^3b^3 + b^2a^4 + ab^5 + b^6 \quad (\text{B25})$$

$$c_8 = (a^4 + b^4) \times c_4 \quad (\text{B26})$$

$$(\text{B27})$$

If $\alpha = \beta$, then the differential equation simplifies to

$$T = R\tau \exp(-\alpha\tau) = R\tau \exp(-a) \quad (\text{B28})$$

Expanding this to 8th order gives

$$T = R\tau \left[1 - a \left(1 - \frac{a}{2} \left(1 - \frac{a}{3} \left(1 - \frac{a}{4} \left(1 - \frac{a}{5} \left(1 - \frac{a}{6} \left(1 - \frac{a}{7} \left(1 - \frac{a}{8} \right)\right)\right)\right)\right)\right)\right)\right] \quad (\text{B29})$$

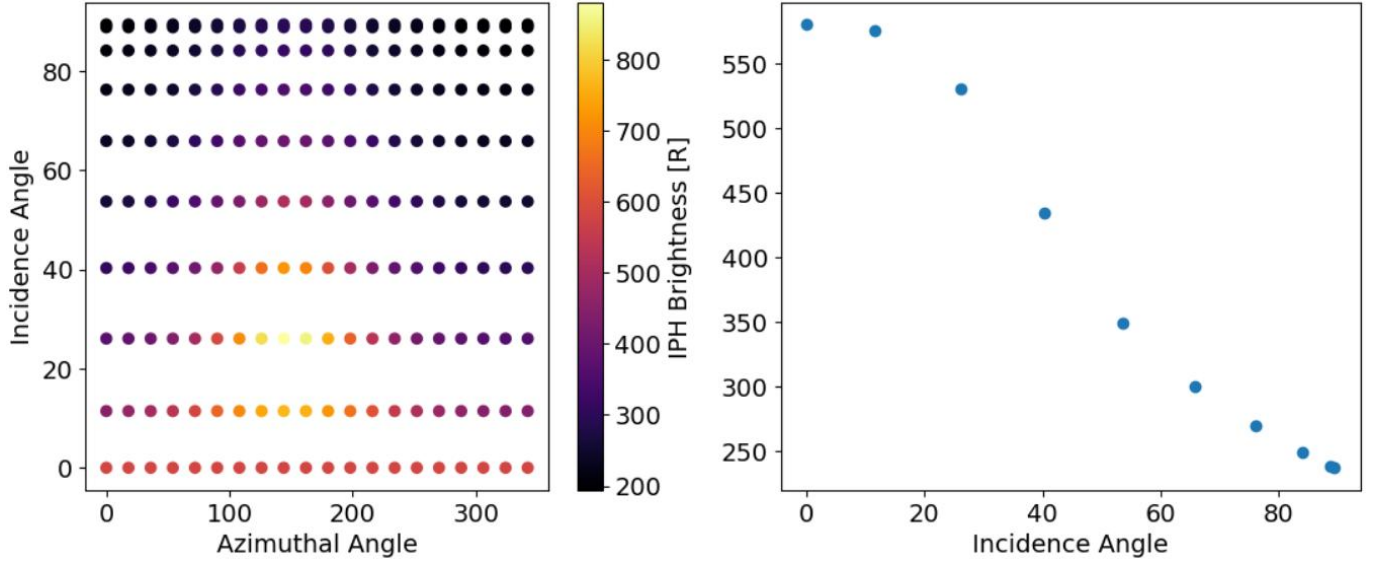


Figure 26. (a) Modelled IPH background brightness as a function of incidence and azimuthal angle for one observation pixel, using the fit in Figure 6. (b) Azimuthally averaged model IPH brightnesses, which are incorporated into the RT model in Eq. C30.

C. MODELLING IPH BRIGHTNESSES

Photons from the interplanetary hydrogen background enter the atmosphere from all directions. Consequently, we integrate over all incidence angles when computing the brightness of IPH scattered by Saturn’s atmosphere, rather than the delta function in incidence angle used for the solar case. As outlined in Section 2.3.2, the IPH brightness is fit with respect to $\cos \theta_{max}$, the angle to the direction of maximum brightness. At 9-10 au, the direction of maximum IPH brightness is closely aligned with the sun direction.

For each pixel, a grid of points is generated around the surface normal (see Fig. 26, spanning both incidence angle and azimuthal direction). The angle of each point to the direction of maximum brightness is computed, and used to calculate the IPH brightness in that direction. This brightness of the IPH incident on the Saturn’s atmosphere is scaled with the 28-day averaged solar flux at the time of observation. We use a Gaussian lineshape at a temperature of 16,000K (Figure 5) in the radiative transfer model. The scattered brightness from the scattered IPH Lyman α photons is given by

$$4\pi I_{IPH}(\mu_{em}) = \Delta\nu_{D,Sat} \times 10^{-6} \int_0^{2\pi} d\phi_{in} \times \int_0^1 d\mu_{in} \int_{-\infty}^{\infty} dx_{in} \int_{-\infty}^{\infty} dx_{em} S(\tau; \mathbf{x}_{em}; \mathbf{x}_{in}) F_{IPH}(\mathbf{x}_{in}) \quad (C30)$$

where we have integrated over all incidence angles. The incident IPH flux is direction dependent such that

$$F_{IPH}(\mathbf{x}_{in}) = B_{IPH}(\mu_{in}, \phi_{in}) \times f_{IPH}(x_{in}, \mu_{in}, \phi_{in}), \quad (C31)$$

where $f_{IPH}(x_{in}, \mu_{in}, \phi_{in})$ is the lineshape, which is normalised to 1. While this does not explicitly depend on the incidence angle, the direction of the normal vector relative to the sunward direction does impact the scattered IPH brightness.

We tested the impact of including a variable IPH Lyman- α lineshift and temperature into the radiative transfer model. We found that this resulted in scattered brightnesses varying by several rayleighs ($\sim 5\%$ of the IPH brightness), which in the context of Saturn is negligible and small compared to the observational uncertainties. Therefore, we simplify $f_{IPH}(x_{in}, \mu_{in}, \phi_{in}) = f_{IPH}(x_{in})$ in Eq. C31.

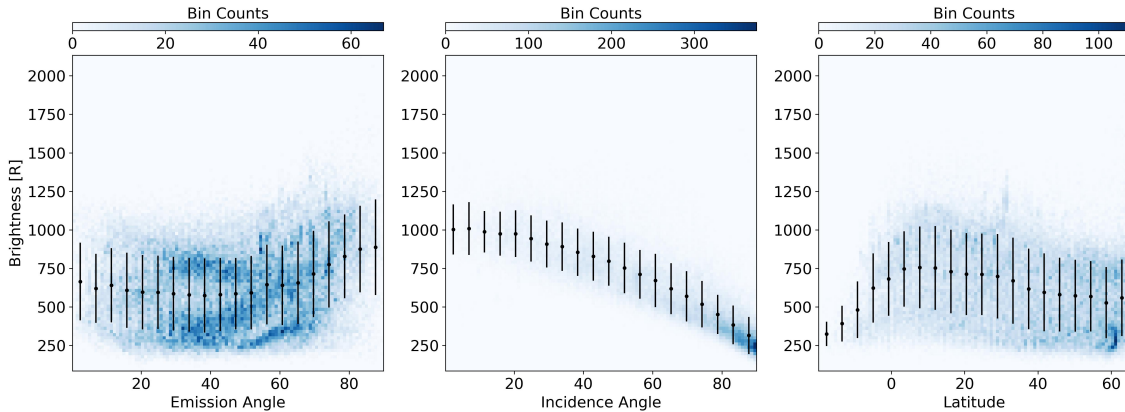


Figure 27. Brightness of the training dataset in the late mission period (2014-2016; see Section 3.2) against emission angle, solar incidence angle and latitude. The median and standard deviations of the observed brightnesses are given in bins of each independent variable.

D. REGRESSION OF THE LYMAN- α BRIGHTNESSES

As described in Section 2.2 and presented in Section 3.2, we have analysed the extensive data set of Lyman- α emission brightnesses throughout the Cassini mission. In this section, we present supplementary material and figures from the regression analyses for the different mission periods.

D.1. Northern hemisphere summer

For the northern hemisphere summer (here taken as 2014-2016), the observed brightnesses show correlations with the emission angle, incidence angle and latitude (see Figure 27). The comparison of the observed and predicted brightnesses for 2014-2016 are shown in Figure 12. We noted that the residuals in Figure 12d show quadratic behaviour, being positive at small and large predicted brightnesses. However, the quadratic behaviour seen in Fig. 28b, is not seen with respect to each independent variable (Figure 28a-c). Therefore, the choice of a combination of quadratic and cubic fits with respect to the independent variables (see Eq. 1) is sufficient to describe the brightnesses.

Figure 29 shows the fits of the multi-variate regression in bins of latitude during the northern hemisphere summer. The variation of the observed brightness with incidence and emission angle is consistent across the full latitude range, and similar to the prediction of the radiative transfer model (see Fig. 14b). The regions of difference with the radiative transfer model can be attributed to poor coverage in the latitude bin (see Figure 30), so the regression model is not well constrained.

D.2. Southern hemisphere summer

Table 2. Coefficients for the fit used in the multi-variate regression (see Eq. 1), for the 2004-2006 observations.

Variable	Coefficient	Mean Value	Confidence Interval
Constant	p_0	5.95×10^2	$(5.93 \times 10^2, 5.96 \times 10^2)$
θ_{em}	p_1	2.61×10^0	$(2.55 \times 10^0, 2.66 \times 10^0)$
θ_{in}	p_2	-8.85×10^0	$(-8.89 \times 10^0, -8.81 \times 10^0)$
ϕ_{lat}	p_3	1.26×10^0	$(1.15 \times 10^0, 1.37 \times 10^0)$
θ_{em}^2	p_4	9.28×10^{-2}	$(9.07 \times 10^{-2}, 9.50 \times 10^{-2})$
$\theta_{em} \cdot \theta_{in}$	p_5	7.08×10^{-3}	$(4.96 \times 10^{-3}, 9.19 \times 10^{-3})$
θ_{in}^2	p_6	-5.28×10^{-2}	$(-5.45 \times 10^{-2}, -5.11 \times 10^{-2})$
ϕ_{lat}^2	p_7	-1.35×10^{-2}	$(-1.61 \times 10^{-2}, -1.09 \times 10^{-2})$
ϕ_{lat}^3	p_8	-1.35×10^{-3}	$(-1.44 \times 10^{-3}, -1.25 \times 10^{-3})$

We apply the multi-variate regression model (see Section 2.2) to the observations in the southern hemisphere summer (2004-2007). The fit coefficients are listed in Table 2. Figure 31 shows the observed Lyman- α brightness during this

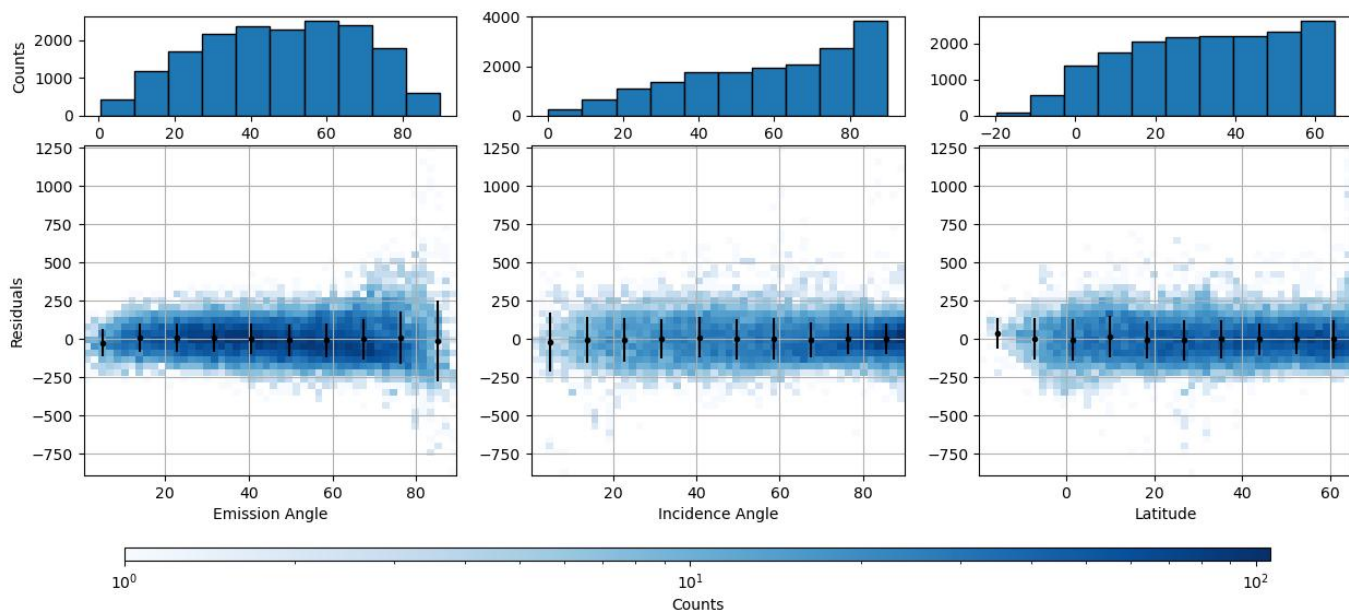


Figure 28. Residuals of the MVR analysis for the testing dataset against each independent variable used in the model for the late mission period (2014-2016). The black points give the mean and standard deviations of the residual brightness.

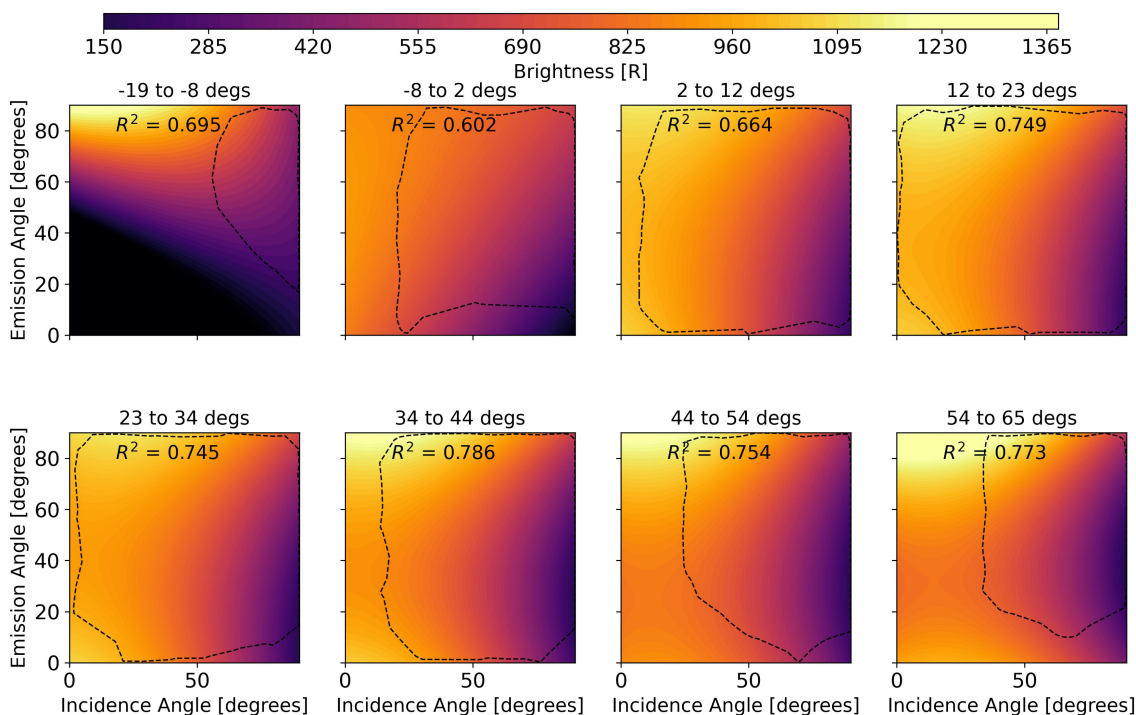


Figure 29. Predicted Lyman- α brightness vs incidence and emission angles in bins of latitude during the northern hemisphere summer (2014-2016). The MVR analysis is applied using a quadratic expression in incidence and emission angles and is trained independently for each latitude bin. The observation coverages in the training datasets are shown in Figure 30.

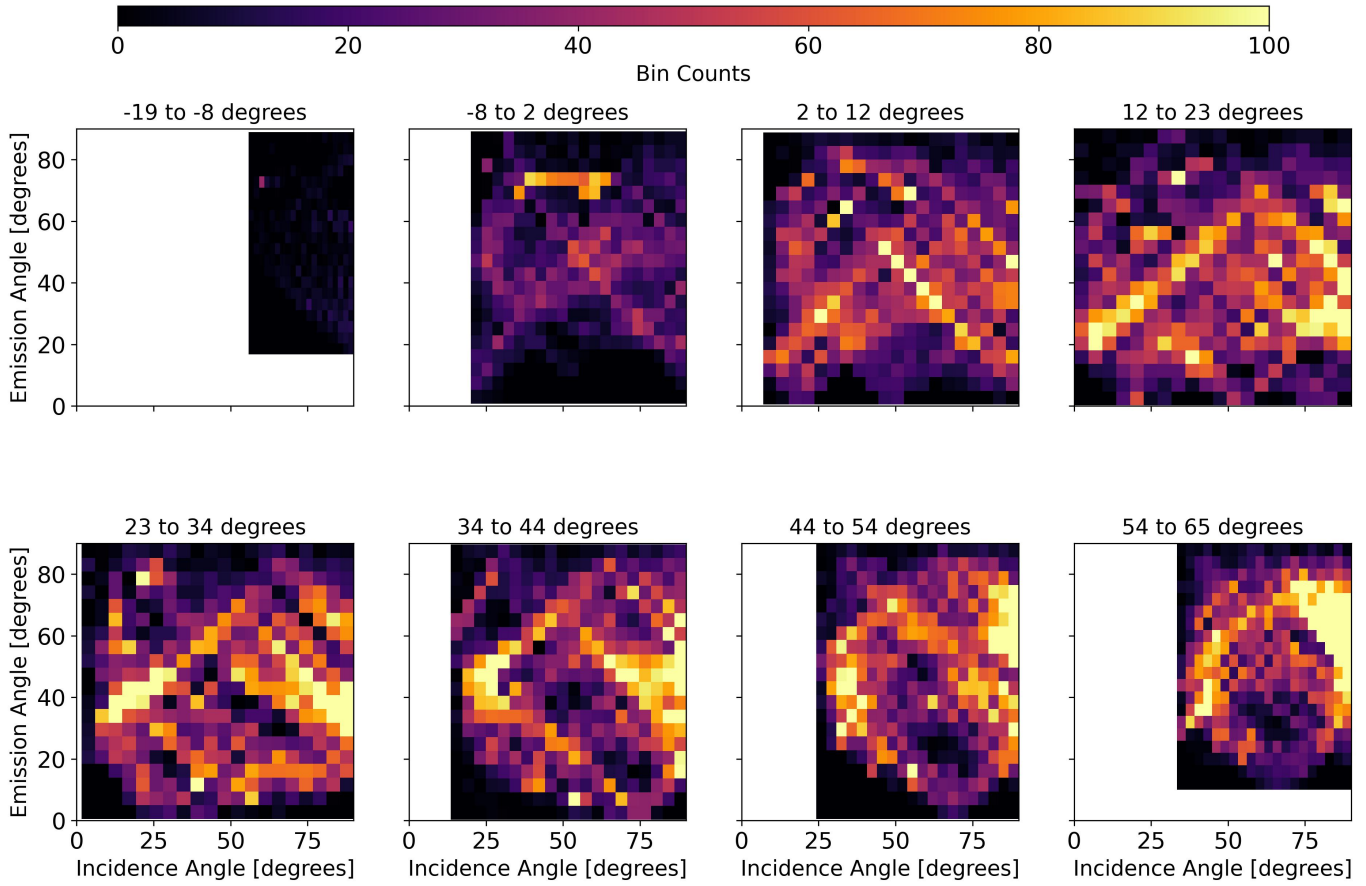


Figure 30. Counts of Lyman- α brightness observations vs incidence and emission angles in bins of latitude during the northern hemisphere summer (2014-2016). The predicted brightnesses from each dataset are shown in Figure 29.

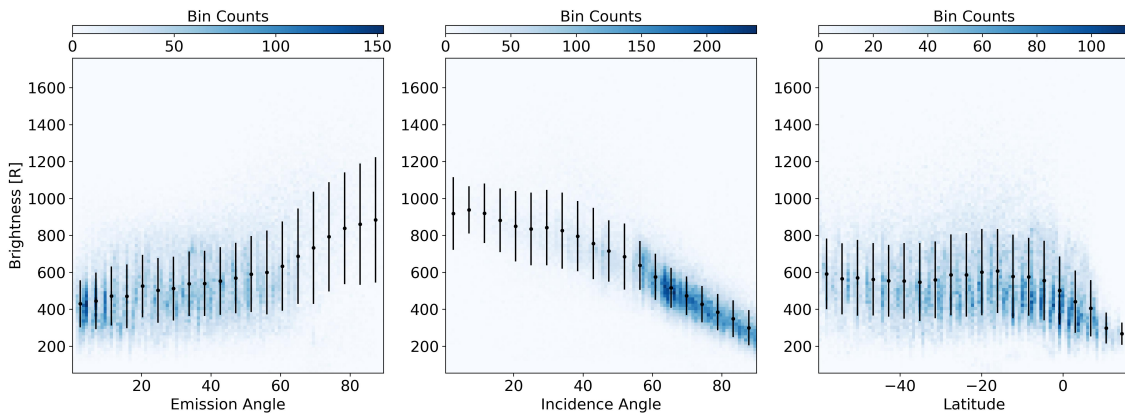


Figure 31. Brightness of the training dataset in the southern hemisphere summer (2004-2007) against emission angle, solar incidence angle and latitude. The median and standard deviations (black) of the observed brightnesses are given in bins of each independent variable.

period, showing similar behaviour with incidence angle and emission angle to that observed in the northern hemisphere summer (see Figure 27). The dependence of the Lyman- α brightness on latitude has reversed, with a peak at -20° and a sharp decrease in brightness in the northern hemisphere. Figure 32 compares the observed brightnesses with predicted brightnesses and residuals. The model accurately reproduces the observed brightnesses between 200 R and

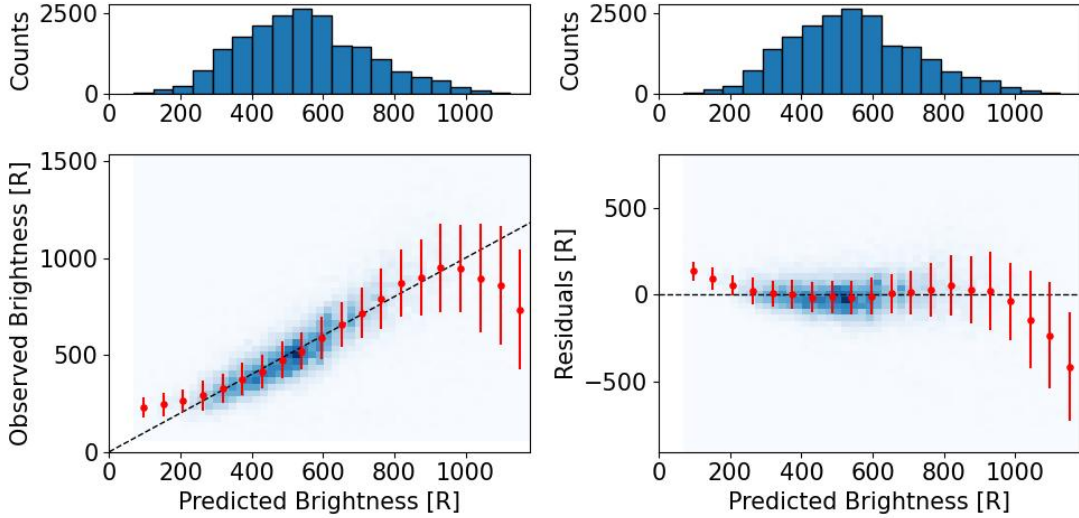


Figure 32. (a,b) Testing data counts vs predicted brightness from the MVR for 2004-2007. (c) Observed brightnesses and (d) residuals vs predicted brightnesses for the testing dataset (blue) with the averages and standard deviations shown in red.

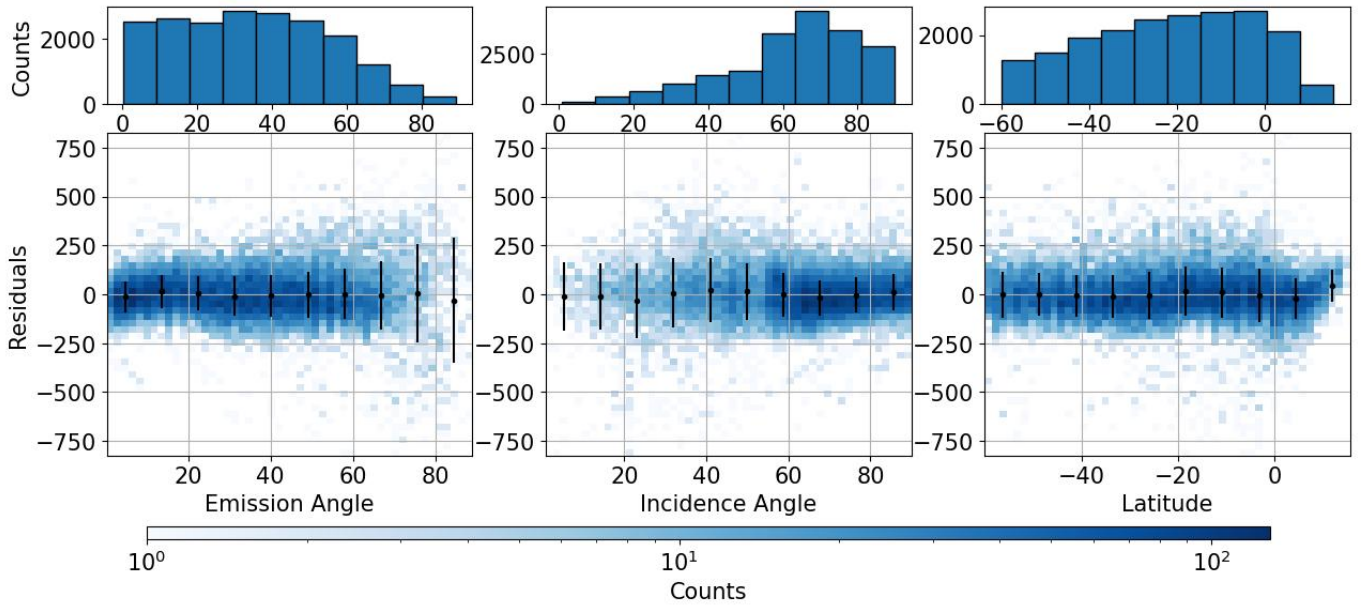


Figure 33. Residuals of the MVR analysis for the testing dataset for 2004-2007 against each independent variable used in the model. The black points give the mean and standard deviations of the residual brightness.

900 R, but overestimates some large brightnesses. There are few counts where the residuals are large, whereas the statistics are much stronger where the residuals are small (< 200 R).

Similar to the northern summer, the quadratic nature of the residuals in Figure 32b are not replicated in the dependences on each independent variable (see Figure 33). The residuals show little dependence on each of the independent variables, suggesting higher order terms are not required to improve the fits.

The dependence of the predicted brightness on the incidence and emission angles at $\phi_{lat} = -20^\circ$ (see Figure 34) is very similar to that seen in the northern hemisphere summer, and to the predictions of the radiative transfer model (see Figure 14).

The same structure in the predicted brightness is retrieved for each latitude bin with a good fit ($R^2 > 0.6$) for all bins in the southern hemisphere, where more observations were available (see Figure 36). Some bins, such as

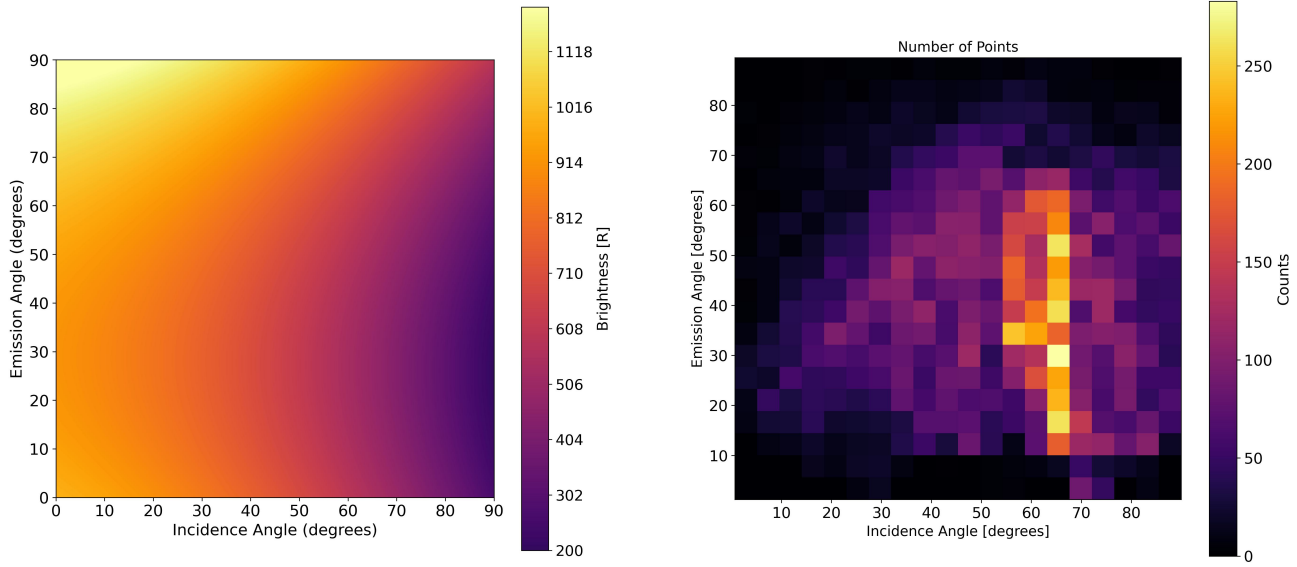


Figure 34. (left) Predicted brightness as a function of solar incidence and emission angles from the MVR analysis at a latitude of -20°N for the 2004-2007 dataset. (right) Observation counts as a function of solar incidence and emission angles used to train the MVR analysis for the 2004-2007 dataset.

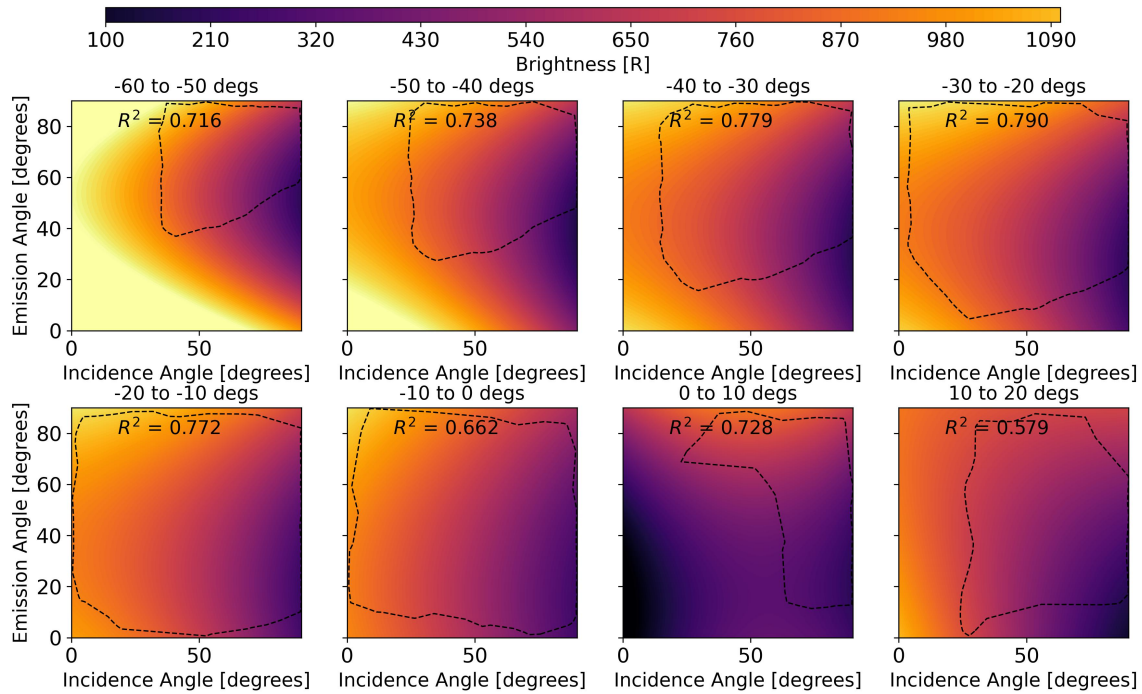


Figure 35. Predicted Lyman- α brightness vs incidence and emission angles in bins of latitude during the southern hemisphere summer (2004-2007). The MVR analysis is applied using a quadratic expression in incidence and emission angles and is trained independently for each latitude bin. The observation coverage in the training dataset are shown in Figure 36.

$\phi_{lat} = [-60, -49]$, predict large brightnesses at low emission angles, contrary to the radiative transfer model. In each of these cases, the data coverage does not extend to low emission angles, so this should not be interpreted physically.

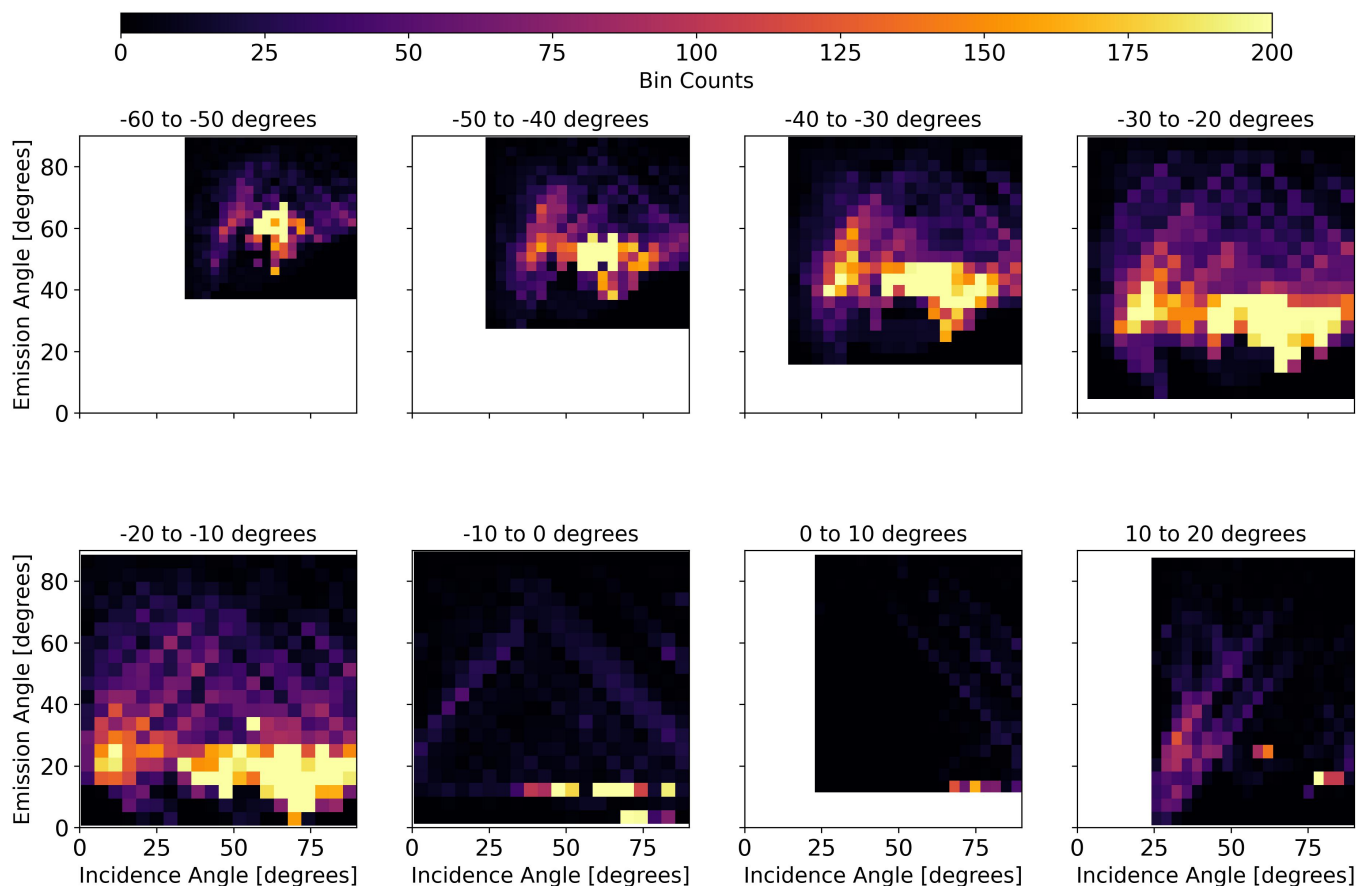


Figure 36. Counts of Lyman- α brightness observations vs incidence and emission angles in bins of latitude during the southern hemisphere summer (2004-2007). The predicted brightnesses from each dataset are shown in Figure 35.

E. ABSORPTION BY THE INTERPLANETARY LYMAN- α

Between 1 au, where the Lyman alpha profile has been measured (Lemaire et al. 2005), and Saturn, the interplanetary hydrogen background absorbs some of the Lyman α , particularly near the line-centre, reducing the line-centre flux by up to 13%. As the flux at line centre is important for resonance scattering, we model the absorption of the IPH background using the IPH model of Quémerais et al. (2013a); Izmodenov et al. (2013), which is discussed in Section 2.3.2.

We calculate the absorption for 36 radial profiles distributed along Saturn’s orbit, relative to the flow of the local interstellar medium. The optical depth of the IPH background is integrated radially to a heliocentric distance of 9.5 au, including the Doppler shift and width of the absorption profile resulting from the bulk IPH velocity.

Using the optical depth, we correct the Lyman- α lineshape and average the absorption profiles around the linecenter. It is assumed that resonance scattering is symmetric about the linecenter in the radiative transfer model, so the absorption must also be made symmetric.

Figure 5 shows the corrected Lyman- α lineshape for the mean absorption profile (dashed black line) with the absorption variability (black shaded region), compared to the flux shape without IPH absorption.

F. IPH OBSERVATIONS

The observations of the Lyman- α IPH background we use in Section 3.1 are listed in Table 3.

REFERENCES

Atreya, S., Waite Jr, J., Donahue, T., Nagy, A., & McConnell, J. C. 1984, Saturn, 239

Atreya, S. K. 1982, Planetary and Space Science, 30, 849, doi: 10.1016/0032-0633(82)90117-9

Table 3. Observations of the IPH Lyman- α background by Cassini/UVIS in 2006, with heliocentric distance (D_H) and background brightness. The right ascension and declination of the observation and the sunward direction (\odot) are given.

Day of year	Lead	D_H	Background [R]	Ly- α [R]	Scaled B [R]	RA	DEC	RA $_{\odot}$	DEC $_{\odot}$
014	CIRS	9.08	4.04 \pm 2.20	251 \pm 72	229 \pm 65	101.7	-2.75	309.91	-19.04
015	UVIS	9.08	5.50 \pm 1.10	557 \pm 61	508 \pm 55	279.1	3.01	309.92	-19.02
	ISS	9.08	5.74 \pm 0.69	596 \pm 39	544 \pm 35	277.4	3.18	309.93	-19.02
	CIRS	9.08	5.80 \pm 0.94	348 \pm 47	317 \pm 42	101.7	-2.75	309.91	-19.03
	CIRS	9.08	5.75 \pm 1.66	202 \pm 14	184 \pm 12	101.2	-2.81	309.92	-19.03
057	VIMS	9.10	5.53 \pm 1.22	183 \pm 12	172 \pm 11	134.2	0.75	311.46	-18.67
058	UVIS	9.10	5.45 \pm 1.67	619 \pm 52	582 \pm 48	309.6	-0.24	311.53	-18.65
	CIRS	9.10	5.40 \pm 0.64	673 \pm 45	633 \pm 42	309.0	-0.17	311.54	-18.65
	ISS	9.10	5.91 \pm 1.04	286 \pm 74	269 \pm 69	133.2	0.64	311.49	-18.66
077	CIRS	9.10	5.47 \pm 1.44	304 \pm 27	288 \pm 25	73.5	-5.12	312.28	-18.52
	ISS	9.10	6.24 \pm 2.71	341 \pm 36	323 \pm 34	72.2	-5.2	312.29	-18.52
078	CIRS	9.09	5.46 \pm 1.70	433 \pm 32	411 \pm 30	248.8	5.42	312.30	-18.51
	VIMS	9.09	4.97 \pm 1.51	444 \pm 15	421 \pm 14	249.5	5.38	312.30	-18.51
121	UVIS	9.11	5.66 \pm 1.33	596 \pm 55	546 \pm 50	282.1	2.72	313.84	-18.12
140	UVIS	9.11	5.27 \pm 1.54	274 \pm 37	250 \pm 33	44.0	-6.31	314.62	-17.97
183	UVIS	9.12	5.78 \pm 1.15	445 \pm 28	416 \pm 26	255.3	4.92	316.14	-17.58
250	CIRS	9.14	5.44 \pm 0.92	333 \pm 21	310 \pm 19	19.2	-15.1	318.67	-16.97
	UVIS	9.14	4.85 \pm 2.06	330 \pm 27	307 \pm 25	20.6	-15.8	318.67	-16.96
	CIRS	9.14	5.52 \pm 1.15	247 \pm 84	229 \pm 78	25.9	-18.0	318.68	-16.96
	ISS	9.14	6.08 \pm 1.12	249 \pm 43	231 \pm 40	204.7	17.6	318.69	-16.96
	ISS	9.14	5.51 \pm 1.37	237 \pm 52	220 \pm 48	205.3	17.8	318.67	-16.96
266	UVIS	9.14	5.10 \pm 0.94	288 \pm 38	267 \pm 35	27.2	-20.6	319.26	-16.81
282	CIRS	9.14	4.73 \pm 1.79	300 \pm 8	279 \pm 7	28.5	-28.5	319.84	-16.66
	CIRS	9.14	5.40 \pm 1.01	337 \pm 15	313 \pm 13	210.2	33.8	319.86	-16.66
283	CIRS	9.14	5.01 \pm 1.12	292 \pm 17	271 \pm 15	208.0	32.3	319.89	-16.64
297	UVIS	9.15	5.43 \pm 0.88	317 \pm 11	298 \pm 10	31.0	-35.3	320.40	-16.52
299	VIMS	9.15	5.73 \pm 1.55	315 \pm 31	296 \pm 29	219.4	36.3	320.44	-16.50
346	UVIS	9.16	5.00 \pm 1.18	293 \pm 33	271 \pm 30	39.6	-38.7	322.15	-16.04
	CIRS	9.16	5.10 \pm 2.15	289 \pm 28	267 \pm 25	215.1	42.9	322.18	-16.02
361	CIRS	9.16	5.37 \pm 1.01	308 \pm 12	288 \pm 11	34.8	-44.6	322.72	-15.88
362	CIRS	9.16	5.21 \pm 0.51	300 \pm 25	281 \pm 23	218.3	48.5	322.74	-15.87
	CIRS	9.16	5.21 \pm 0.84	286 \pm 22	268 \pm 20	219.2	49.6	322.75	-15.87

Barker, E., Cazes, S., Emerich, C., et al. 1980, ApJ, 242, 383, doi: [10.1086/158471](https://doi.org/10.1086/158471)

Barth, C. A., Rusch, D. W., Thomas, R. J., et al. 1983, Geophysical Research Letters, 10, 237, doi: [10.1029/GL010I004P00237](https://doi.org/10.1029/GL010I004P00237)

Ben-Jaffel, L., Moses, J. I., West, R. A., et al. 2023, The Planetary Science Journal, 4, 54, doi: [10.3847/PSJ/ACAF78](https://doi.org/10.3847/PSJ/ACAF78)

Ben-Jaffel, L., Prangé, R., Sandel, B. R., et al. 1995, Icarus, 113, 91, doi: [10.1006/ICAR.1995.1007](https://doi.org/10.1006/ICAR.1995.1007)

Broadfoot, A. L., Sandel, B. R., Shemansky, D. E., et al. 1981, Science, 212, 206, doi: [10.1126/SCIENCE.212.4491.206](https://doi.org/10.1126/SCIENCE.212.4491.206)

Brown, Z., Koskinen, T., Müller-Wodarg, I., et al. 2020, Nature Astronomy 2020 4:9, 4, 872, doi: [10.1038/s41550-020-1060-0](https://doi.org/10.1038/s41550-020-1060-0)

Brown, Z. L., Koskinen, T. T., Moses, J., & Guerlet, S. 2024, Icarus

Brown, Z. L., Medvedev, A. S., Starichenko, E. D., Koskinen, T. T., & Müller-Wodarg, I. C. 2022, Geophysical Research Letters, 49, e2021GL097219, doi: [10.1029/2021GL097219](https://doi.org/10.1029/2021GL097219)

Bzowski, M., Möbius, E., Tarnopolski, S., Izmodenov, V., & Gloeckler, G. 2009, Space Science Reviews, 143, 177, doi: [10.1007/S11214-008-9479-0/METRICS](https://doi.org/10.1007/S11214-008-9479-0/METRICS)

- Chen, F. Z., & Wu, C. Y. 2004, *Journal of Quantitative Spectroscopy and Radiative Transfer*, 85, 195, doi: [10.1016/S0022-4073\(03\)00225-5](https://doi.org/10.1016/S0022-4073(03)00225-5)
- Clarke, J. T., Moos, H. W., Atreya, S. K., & Lane, A. L. 1981, *Nature* 1981 290:5803, 290, 226, doi: [10.1038/290226a0](https://doi.org/10.1038/290226a0)
- Clarke, J. T., Weaver, H. A., Feldman, P. D., et al. 1980, *The Astrophysical Journal*, 240, 696, doi: [10.1086/158277](https://doi.org/10.1086/158277)
- Dessler, A. J., Sandel, B. R., & Atreya, S. K. 1981, *Planetary and Space Science*, 29, 215, doi: [10.1016/0032-0633\(81\)90035-0](https://doi.org/10.1016/0032-0633(81)90035-0)
- Dialynas, K., Krimigis, S. M., Decker, R. B., & Mitchell, D. G. 2019, *Geophysical Research Letters*, 46, 7911, doi: [10.1029/2019GL083924](https://doi.org/10.1029/2019GL083924)
- Emerich, C., Ben Jaffel, L., & Prangé, R. 1993, *Planetary and Space Science*, 41, 363, doi: [10.1016/0032-0633\(93\)90070-I](https://doi.org/10.1016/0032-0633(93)90070-I)
- Esposito, L. W., Barth, C. A., Colwell, J. E., et al. 2005, *Space Science Reviews*, 115, 299, doi: [10.1007/S11214-004-1455-8](https://doi.org/10.1007/S11214-004-1455-8)
- Fasar, F. M., Kunde, V. G., Abbas, M. M., et al. 2005, *Space Science Reviews*, 115, 169, doi: [10.1007/S11214-004-1454-9](https://doi.org/10.1007/S11214-004-1454-9)
- Gladstone, G. R., Pryor, W. R., Stern, S. A., et al. 2018, *Geophysical Research Letters*, 45, 8022, doi: [10.1029/2018GL078808](https://doi.org/10.1029/2018GL078808)
- Gladstone, G. R., Pryor, W. R., Hall, D. T., et al. 2021, doi: [10.3847/1538-3881/ac23cd](https://doi.org/10.3847/1538-3881/ac23cd)
- Guerlet, S., Fouchet, T., Spiga, A., et al. 2018, *Journal of Geophysical Research: Planets*, 123, 246, doi: [10.1002/2017JE005419](https://doi.org/10.1002/2017JE005419)
- Gustin, J., Stewart, I., Gérard, J. C., & Esposito, L. 2010, *Icarus*, 210, 270, doi: [10.1016/j.icarus.2010.06.031](https://doi.org/10.1016/j.icarus.2010.06.031)
- Hinteregger, H. E., Fukui, K., & Gilson, B. R. 1981, *Geophysical Research Letters*, 8, 1147, doi: [10.1029/GL008I011P01147](https://doi.org/10.1029/GL008I011P01147)
- Hue, V., Cavalié, T., Dobrijevic, M., Hersant, F., & Greathouse, T. K. 2015, *Icarus*, 257, 163, doi: [10.1016/J.ICARUS.2015.04.001](https://doi.org/10.1016/J.ICARUS.2015.04.001)
- Hue, V., Greathouse, T. K., Cavalié, T., Dobrijevic, M., & Hersant, F. 2016, *Icarus*, 267, 334, doi: [10.1016/J.ICARUS.2015.12.007](https://doi.org/10.1016/J.ICARUS.2015.12.007)
- Hummer, D. G. 1962, *Monthly Notices of the Royal Astronomical Society*, 125, 21, doi: [10.1093/MNRAS/125.1.21](https://doi.org/10.1093/MNRAS/125.1.21)
- Izmodenov, V. V., & Alexashov, D. B. 2020, *Astronomy & Astrophysics*, 633, L12, doi: [10.1051/0004-6361/201937058](https://doi.org/10.1051/0004-6361/201937058)
- Izmodenov, V. V., Gruntman, M., & Malama, Y. G. 2001, *Journal of Geophysical Research: Space Physics*, 106, 10681, doi: [10.1029/2000JA000273](https://doi.org/10.1029/2000JA000273)
- Izmodenov, V. V., Katushkina, O. A., Quémerais, E., & Bzowski, M. 2013, *Cross-Calibration of Far UV Spectra of Solar System Objects and the Heliosphere*, 7, doi: [10.1007/978-1-4614-6384-9_{_}2](https://doi.org/10.1007/978-1-4614-6384-9_{_}2)
- Katushkina, O. A., Quémerais, E., Izmodenov, V. V., Alexashov, D. B., & Sandel, B. R. 2016, *Journal of Geophysical Research: Space Physics*, 121, 93, doi: [10.1002/2015JA022062](https://doi.org/10.1002/2015JA022062)
- Katushkina, O. A., Quémerais, E., Izmodenov, V. V., Lallement, R., & Sandel, B. R. 2017, *Journal of Geophysical Research: Space Physics*, 122, 921, doi: [10.1002/2017JA024205](https://doi.org/10.1002/2017JA024205)
- Koskinen, T. T., & Guerlet, S. 2018, *Icarus*, 307, 161, doi: [10.1016/j.icarus.2018.02.020](https://doi.org/10.1016/j.icarus.2018.02.020)
- Koskinen, T. T., Moses, J. I., West, R. A., Guerlet, S., & Jouchoux, A. 2016, *Geophysical Research Letters*, 43, 7895, doi: [10.1002/2016GL070000](https://doi.org/10.1002/2016GL070000)
- Koskinen, T. T., Sandel, B. R., Yelle, R. V., et al. 2013, *Icarus*, 226, 1318, doi: [10.1016/J.ICARUS.2013.07.037](https://doi.org/10.1016/J.ICARUS.2013.07.037)
- Koskinen, T. T., Sandel, B. R., Yelle, R. V., Holsclaw, G. M., & Quemerai, E. 2020, *Icarus*, 339, 113594, doi: [10.1016/J.ICARUS.2019.113594](https://doi.org/10.1016/J.ICARUS.2019.113594)
- Koskinen, T. T., Sandel, B. R., Yelle, R. V., et al. 2015, *Icarus*, 260, 174, doi: [10.1016/J.ICARUS.2015.07.008](https://doi.org/10.1016/J.ICARUS.2015.07.008)
- Koskinen, T. T., Strobel, D. F., & Brown, Z. 2021, *Icarus*, 362, doi: [10.1016/j.icarus.2021.114396](https://doi.org/10.1016/j.icarus.2021.114396)
- Krstić, P. S., & Schultz, D. R. 1999, *Physical Review A*, 60, 2118, doi: [10.1103/PhysRevA.60.2118](https://doi.org/10.1103/PhysRevA.60.2118)
- Larsson, M., McCall, B. J., & Orel, A. E. 2008, *Chemical Physics Letters*, 462, 145, doi: [10.1016/j.cplett.2008.06.069](https://doi.org/10.1016/j.cplett.2008.06.069)
- Lemaire, P., Emerich, C., Vial, J. C., et al. 2005, *Advances in Space Research*, 35, 384, doi: [10.1016/j.asr.2004.11.004](https://doi.org/10.1016/j.asr.2004.11.004)
- Machol, J., Snow, M., Woodraska, D., et al. 2019, *Earth and Space Science*, 6, 2263, doi: [10.1029/2019EA000648](https://doi.org/10.1029/2019EA000648)
- Matson, D. L., Spilker, L. J., & Lebreton, J. P. 2002, *Space Science Reviews*, 104, 1, doi: [10.1023/A:1023609211620](https://doi.org/10.1023/A:1023609211620)
- McClintock, W. E., Snow, M., & Woods, T. N. 2005, *The Solar Radiation and Climate Experiment (SORCE): Mission Description and Early Results*, 230, 259, doi: [10.1007/0-387-37625-9_{_}13/COVER](https://doi.org/10.1007/0-387-37625-9_{_}13/COVER)
- McGrath, M. A., & Clarke, J. T. 1992, *Journal of Geophysical Research: Space Physics*, 97, 13691, doi: [10.1029/92JA00143](https://doi.org/10.1029/92JA00143)
- Mitchell, D. G., Kurth, W. S., Hospodarsky, G. B., et al. 2009, *Journal of Geophysical Research: Space Physics*, 114, n/a, doi: [10.1029/2008JA013621](https://doi.org/10.1029/2008JA013621)

- Moses, J. I., & Bass, S. F. 2000, *Journal of Geophysical Research: Planets*, 105, 7013, doi: [10.1029/1999JE001172](https://doi.org/10.1029/1999JE001172)
- Moses, J. I., Bézard, B., Lellouch, E., et al. 2000a, *Icarus*, 143, 244, doi: [10.1006/icar.1999.6270](https://doi.org/10.1006/icar.1999.6270)
- Moses, J. I., & Greathouse, T. K. 2005, *Journal of Geophysical Research: Planets*, 110, 1, doi: [10.1029/2005JE002450](https://doi.org/10.1029/2005JE002450)
- Moses, J. I., Lellouch, E., Bézard, B., et al. 2000b, *Icarus*, 145, 166, doi: [10.1006/icar.1999.6320](https://doi.org/10.1006/icar.1999.6320)
- Moses, J. I., Brown, Z. L., Koskinen, T. T., et al. 2023, *Icarus*, 391, 115328, doi: [10.1016/J.ICARUS.2022.115328](https://doi.org/10.1016/J.ICARUS.2022.115328)
- Müller-Wodarg, I. C., Koskinen, T. T., Moore, L., et al. 2019, *Geophysical Research Letters*, 46, 2372, doi: [10.1029/2018GL081124](https://doi.org/10.1029/2018GL081124)
- O'Donoghue, J., Moore, L., Connerney, J., et al. 2019, *Icarus*, 322, 251, doi: [10.1016/J.ICARUS.2018.10.027](https://doi.org/10.1016/J.ICARUS.2018.10.027)
- Pryor, W. R., Gladstone, G. R., Retherford, K. D., & Tobiska, W. K. 2022, *The Astronomical Journal*, 164, 46, doi: [10.3847/1538-3881/AC7570](https://doi.org/10.3847/1538-3881/AC7570)
- Pryor, W. R., Gladstone, G. R., Retherford, K. D., et al. 2024, *The Astrophysical Journal*, 960, 117, doi: [10.3847/1538-4357/AD1181](https://doi.org/10.3847/1538-4357/AD1181)
- Quémerais, E. 2000, *A&A*, 358, 353. <https://ui.adsabs.harvard.edu/abs/2000A&A...358..353Q/abstract>
- Quémerais, E., Bertaux, J. L., Lallement, R., Sandel, B. R., & Izmodenov, V. 2003, *Journal of Geophysical Research: Space Physics*, 108, doi: [10.1029/2003JA009871](https://doi.org/10.1029/2003JA009871)
- Quémerais, E., & Izmodenov, V. 2002, *Astronomy and Astrophysics*, 396, 269, doi: [10.1051/0004-6361:20021396](https://doi.org/10.1051/0004-6361:20021396)
- Quémerais, E., Lallement, R., Ferron, S., et al. 2006, *JGRA*, 111, A09114, doi: [10.1029/2006ja011711](https://doi.org/10.1029/2006ja011711)
- Quémerais, E., Sandel, B. R., Izmodenov, V. V., & Gladstone, G. R. 2013a, *Cross-Calibration of Far UV Spectra of Solar System Objects and the Heliosphere*, 141, doi: [10.1007/978-1-4614-6384-9_4/COVER](https://doi.org/10.1007/978-1-4614-6384-9_4/COVER)
- Quémerais, E., Snow, M., & Bonnet, R. M. 2013b, *Cross-Calibration of Far UV Spectra of Solar System Objects and the Heliosphere*, 1, doi: [10.1007/978-1-4614-6384-9](https://doi.org/10.1007/978-1-4614-6384-9)
- Quémerais, E., Chaufray, J. Y., Koutroumpa, D., et al. 2020, *Space Science Reviews*, 216, 1, doi: [10.1007/S11214-020-00695-6/FIGURES/10](https://doi.org/10.1007/S11214-020-00695-6/FIGURES/10)
- Sandel, B. R., Broadfoot, A. L., & Strobel, D. F. 1980, *Geophysical Research Letters*, 7, 5, doi: [10.1029/GL007I001P00005](https://doi.org/10.1029/GL007I001P00005)
- Sandel, B. R., Shemansky, D. E., Broadfoot, A. L., et al. 1982, *Science*, 215, 548, doi: [10.1126/SCIENCE.215.4532.548](https://doi.org/10.1126/SCIENCE.215.4532.548)
- Serigano, J., Hörst, S. M., He, C., et al. 2020, *Journal of Geophysical Research: Planets*, 125, e2020JE006427, doi: [10.1029/2020JE006427](https://doi.org/10.1029/2020JE006427)
- . 2022, *Journal of Geophysical Research: Planets*, 127, e2022JE007238, doi: [10.1029/2022JE007238](https://doi.org/10.1029/2022JE007238)
- Shemansky, D. E., & Liu, X. 2012, *Canadian Journal of Physics*, 90, 817, doi: [10.1139/P2012-036](https://doi.org/10.1139/P2012-036)
- Shemansky, D. E., Liu, X., & Melin, H. 2009, *Planetary and Space Science*, 57, 1659, doi: [10.1016/J.PSS.2009.05.002](https://doi.org/10.1016/J.PSS.2009.05.002)
- Skinner, T. E., DeLand, M. T., Ballester, G. E., et al. 1988, *Journal of Geophysical Research: Space Physics*, 93, 29, doi: [10.1029/JA093IA01P00029](https://doi.org/10.1029/JA093IA01P00029)
- Swaczyna, P., McComas, D. J., Zirnstein, E. J., et al. 2020, *The Astrophysical Journal*, 903, 48, doi: [10.3847/1538-4357/ABB80A](https://doi.org/10.3847/1538-4357/ABB80A)
- Waite, J. H., Cravens, T. E., Kozyra, J., et al. 1983, *Journal of Geophysical Research: Space Physics*, 88, 6143, doi: <https://doi.org/10.1029/JA088iA08p06143>
- Waite, J. H., Perryman, R. S., Perry, M. E., et al. 2018, *Science*, 362, doi: [10.1126/SCIENCE.AAT2382/ASSET/957EE0D9-032D-4345-AAE8-E3D27A359968/ASSETS/GRAPHIC/362_{-}AAT2382_{-}F8.JPEG](https://doi.org/10.1126/SCIENCE.AAT2382/ASSET/957EE0D9-032D-4345-AAE8-E3D27A359968/ASSETS/GRAPHIC/362_{-}AAT2382_{-}F8.JPEG)
- Wallace, L., Yelle, R. V., Wallace, L., & Yelle, R. V. 1989, *ApJ*, 346, 489, doi: [10.1086/168030](https://doi.org/10.1086/168030)
- Weiser, H., Vitz, R. C., & Moos, H. W. 1977, *Science*, 197, 755, doi: [10.1126/SCIENCE.197.4305.755](https://doi.org/10.1126/SCIENCE.197.4305.755)
- Woods, T. N., Tobiska, W. K., Rottman, G. J., & Worden, J. R. 2000, *Journal of Geophysical Research: Space Physics*, 105, 27195, doi: [10.1029/2000JA000051](https://doi.org/10.1029/2000JA000051)
- Yelle, R. V. 1988, *Astrophysical Journal* v.332, p.514, 332, 514, doi: [10.1086/166673](https://doi.org/10.1086/166673)
- Yelle, R. V., Sandel, B. R., Shemansky, D. E., & Kumar, S. 1986, *Journal of Geophysical Research: Space Physics*, 91, 8756, doi: [10.1029/JA091IA08P08756](https://doi.org/10.1029/JA091IA08P08756)
- Yelle, R. V., Serigano, J., Koskinen, T. T., et al. 2018, *Geophysical Research Letters*, 45, 951, doi: [10.1029/2018GL078454](https://doi.org/10.1029/2018GL078454)
- Yelle, R. V., & Wallace, L. 1989, *Astrophysical Journal*, Part 1, 346, 481. <https://adsabs.harvard.edu/full/1989ApJ...346..481Y>
- Yelle, R. V., Wallace, L., Yelle, R. V., & Wallace, L. 1989, *ApJ*, 346, 481, doi: [10.1086/168029](https://doi.org/10.1086/168029)